Pulsed Electron–Nuclear Double Resonance Methodology

CLAUDIUS GEMPERLE and ARTHUR SCHWEIGER*

Laboratorium für Physikalische Chemie, Eidgenössische Technische Hochschule, 8092 Zürich, Switzerland

Received April 1, 1991 (Revised Manuscript Received July 18, 1991)

Contents

Claudius Gemperle was born in St. Gallen, Switzerland, in 1961. He studied Chemistry at the Swiss Federal Institute of Technology (ETH) in Zurich. In 1990 he completed his Ph.D. studies under the direction of R. R. Ernst with a thesis about electron spin echo methodology. His research interests include the theory and application of magnetic resonance, and analytical chemistry.

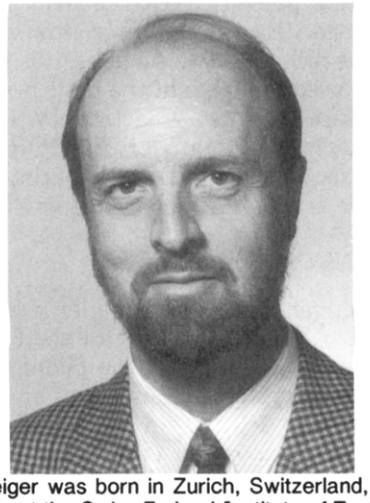

Arthur Schweiger was born in Zurich, Switzerland, in 1946. He studied Physics at the Swiss Federal Institute of Technology (ETH) in Zurich and received his Ph.D. in 1976, studying under the guidance of Hs. H. Günthard. He then joined the Magnetic Resonance Group of the Laboratory for Physical Chemistry at ETH, where he presently is a Professor of Physical Chemistry. His major fields of scientific interests are the methodology of ESR spectroscopy and the application of ESR in coordination chemistry.

I. Introduction

Electron–nuclear double resonance (ENDOR) is a *well-established magnetic resonance technique for ob*taining detailed molecular and electronic structure information about paramagnetic species.[1–7] In the classical continuous wave (cw) ENDOR experiment an ESR transition is saturated with an intense microwave (mw) field. A second irradiating field in the radio frequency (rf) region induces nuclear spin transitions, thereby altering the populations of some of the energy levels. These changes are then detected by observing the variations in the polarization of the saturated ESR transition. Since in ENDOR the NMR spectrum of a paramagnetic compound is measured indirectly via the electron spin, the sensitivity of ENDOR is much higher than that obtained in an NMR experiment. The main advantage of ENDOR, however, consists in the substantial improvement in resolution that can be achieved relative to ESR. This resolution enhancement is caused by the introduction of additional selection rules and may amount to several orders of magnitude. It is therefore not surprising that cw ENDOR, with its extensive armory of sophisticated techniques,[3,4,8] has developed into one of the cornerstones of electron spin resonance.

It was as early as 1965, when Bill Mims demonstrated that ENDOR experiments can also be carried out with *pulsed* mw and rf excitation.[9] In such a pulsed ENDOR experiment, the intensity of the electron spin echo is measured as a function of the radio frequency. During the first two decades after invention of pulsed ENDOR, the capabilities of the method were not much noticed by the ESR community. This is demonstrated by the small number of papers published about the subject in this period.[10–17] Along with the rapid developments in

0009-2665/91/0791-1481$09.50/0

pulsed ESR spectroscopy in the last several years,[18-24] however, there has also been a fast growing interest in the related pulsed ENDOR technique.[25-43] One of the advantages of pulsed ENDOR compared with the cw ENDOR method is that the entire sequence can usually be made short enough to exclude unwanted relaxation effects. Moreover, the ENDOR efficiency in the pulsed version can be up to 100%, whereas in the cw approach, ENDOR signal intensities are only a few percent of those with ESR. This high efficiency, however, does not necessarily mean that in any case pulsed ENDOR is more sensitive than cw ENDOR, because the cw ESR signal is usually more intense than the electron spin echo. In pulsed ENDOR, there are also more ways to manipulate the electron–nuclear spin system and, thus, to simplify or unravel complicated spectra than in cw ENDOR. The reputation that pulsed ENDOR has earned in this time is also expressed in a number of recent review articles.[44-47]

In this account, the different pulsed ENDOR techniques invented so far are presented within the frame work of an elegant and transparent operator formalism. This systematic approach allows one to call special attention to the common basis as well as to the diversities of the various methods. Since we mainly concentrate on techniques rather than on applications, experimental results are only presented for illustrative purposes. Section II provides some background knowledge about the ENDOR spectrum of different types of spin systems. To guide the reader through all the burdens of electron–nuclear spin acrobatics involved in the different pulsed ENDOR schemes, we then develop in section III the operator formalism in some detail. In the following two sections, this mathematical apparatus is used to highlight the basic principles of the different pulse schemes. Section IV is devoted to various polarization transfer ENDOR techniques, whereas in section V, ENDOR experiments that are based on the transfer of coherence will be discussed.

II. The ENDOR Spectrum

For the convenience of the reader, we briefly summarize some of the expressions for the ENDOR transition frequencies. Consider the Hamiltonian for an anisotropic spin system consisting of an electron spin $S = {}^1/_2$ and one nuclear spin I

$$\mathcal{H}_0 = \mathcal{H}_{EZ} + \mathcal{H}_{NZ} + \mathcal{H}_{HFS} + \mathcal{H}_Q = \beta_e \mathbf{B}_0 \underline{\underline{\mathbf{g}}} \mathbf{S} - g_n \beta_n \mathbf{B}_0 \mathbf{I} + \mathbf{S}\underline{\underline{\mathbf{A}}}\mathbf{I} + \mathbf{I}\underline{\underline{\mathbf{Q}}}\mathbf{I} \quad (1)$$

The four terms in eq 1 describe the electron Zeeman, the nuclear Zeeman, the hyperfine, and the nuclear quadrupole interaction. Under the assumption $\mathcal{H}_{EZ} \gg \mathcal{H}_{HFS} \gg \mathcal{H}_Q$, the first-order ENDOR angular frequencies may be expressed by[4,48]

$$\omega_{ENDOR}(m_S, m_I + 1 \leftrightarrow m_I) = c(m_S) + {}^3/_2(2m_I + 1)\tilde{Q}(m_S) \quad (2)$$

with

$$c(m_S) = |[\tilde{\ell}\underline{\underline{\mathbf{C}}}(m_S)\tilde{\underline{\underline{\mathbf{C}}}}(m_S)\ell]^{1/2}| \quad (3a)$$

$$\underline{\underline{\mathbf{C}}}(m_S) = g^{-1} m_S \underline{\underline{\mathbf{g}}}\underline{\underline{\mathbf{A}}} + \omega_I \underline{\underline{\mathbf{E}}} \quad (3b)$$

$$g = |[\tilde{\ell}\underline{\underline{\mathbf{g}}}\tilde{\underline{\underline{\mathbf{g}}}}\ell]^{1/2}| \quad (3c)$$

and

$$\tilde{Q}(m_S) = \tilde{\ell}\underline{\underline{\mathbf{C}}}(m_S)\underline{\underline{\mathbf{Q}}}\tilde{\underline{\underline{\mathbf{C}}}}(m_S)\ell / c^2(m_S) \quad (3d)$$

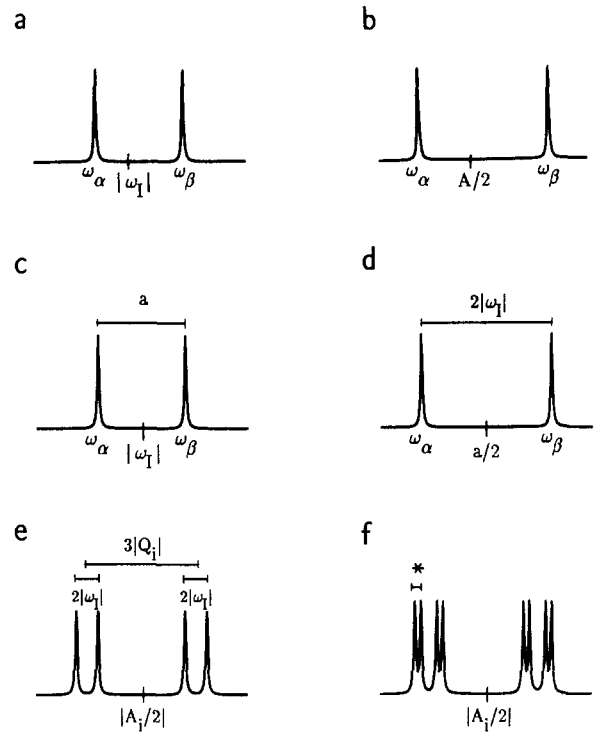

Figure 1. Typical ENDOR spectra of simple $S = {}^1/_2$, I spin systems, $\omega_I < 0$: (a,b) $I = {}^1/_2$; anisotropic spin system, $A > 0$; (a) $|A/2| < |\omega_I|$, (b) $|A/2| > |\omega_I|$; (c,d) $I = {}^1/_2$; isotropic spin system, $a > 0$; $|a/2| < |\omega_I|$ (c), $|a/2| > |\omega_I|$ (d); (e) $I = 1$; anisotropic spin system, B_0 along one of the principal axes of the hyperfine tensor, $|A_i/2| > |\omega_I|$; (f) $I_1 = 1$, $I_2 = 1$; anisotropic spin system, $\mathbf{B}_0$ along one of the principal axes of the hyperfine tensor, $|A_i/2| > |\omega_I|$; the asterisk (*) marks second-order splitting.

In eq 3, $\omega_I = -g_n\beta_n B_0/\hbar$ denotes the nuclear Zeeman frequency, $\underline{\underline{\mathbf{E}}}$ is a 3 × 3 unit matrix and ℓ is the unit vector along the external static field $\mathbf{B}_0$ in the frame spanned by the $\underline{\underline{\mathbf{g}}}$ tensor principal axes. (The negative sign in the expression for ω_I results from the solution of the equation of motion, $\omega_I = -\gamma_n B_0$, and from $\gamma_n = g_n\beta_n/\hbar$). An expansion of these formulas to an arbitrary number of nuclei is straightforward.[48]

A. $I = {}^1/_2$

For a $I = {}^1/_2$ nucleus, the ENDOR transition frequencies in the two m_S manifolds (α- and β-state of the electron spin) are given by

$$\omega_{ENDOR}(m_S = {}^1/_2) = \omega_\alpha = c({}^1/_2)$$

$$\omega_{ENDOR}(m_S = -{}^1/_2) = \omega_\beta = c(-{}^1/_2) \quad (4)$$

The spectra for the two cases $|A/2| < |\omega_I|$ and $|A/2| > |\omega_I|$ with A denoting the hyperfine coupling for a particular direction of $\mathbf{B}_0$ are shown in Figure 1, parts a and b. For an arbitrary orientation of $\mathbf{B}_0$, the splitting of the two ENDOR lines, $|\omega_\beta - \omega_\alpha|$, depends on $\underline{\underline{\mathbf{A}}}$ and $\underline{\underline{\mathbf{g}}}$. It is a consequence of the anisotropy of $\underline{\underline{\mathbf{g}}}$ and $\underline{\underline{\mathbf{A}}}$ that the two lines are not, in general, symmetric about $|\omega_I|$ (for $|A/2| < |\omega_I|$) or $A/2$ (for $|A/2| > |\omega_I|$), but are shifted to higher frequencies.

If the $\underline{\underline{\mathbf{g}}}$ tensor and the $\underline{\underline{\mathbf{A}}}$ tensor are isotropic, eq 4 reduces to

$$\omega_\alpha = |(a/2) + \omega_I|$$

$$\omega_\beta = |(a/2) - \omega_I| \quad (5)$$

where a denotes the isotropic hyperfine coupling constant (Figure 1, parts c and d). A corresponding expression is found for the case where $\mathbf{B}_0$ is oriented along one of the principal axes of the hyperfine tensor (coaxial with $\underline{\underline{g}}$) with principal values A_i, $i = x, y, z$:

$$\omega_\alpha = |(A_i/2) + \omega_I|$$
$$\omega_\beta = |(A_i/2) - \omega_I| \quad (6)$$

For N equivalent $I = {}^1/_2$ nuclei, the ENDOR spectrum still consists of two transitions ($N + 1$ transitions in the ESR spectrum), whereas for N nonequivalent $I = {}^1/_2$ nuclei, $2N$ ENDOR transitions are observed (2^N transitions in the ESR spectrum).

B. $I \geq 1$

For nuclei with $I \geq 1$, the nuclear quadrupole interaction causes a first order splitting of the ENDOR lines. The ENDOR spectrum of an $I = 1$ nucleus consists of four transitions at frequencies

$$\omega_{ENDOR}(m_S) = c(m_S) \pm {}^3/_2\bar{Q}(m_S) \quad (7)$$

For $\mathbf{B}_0$ along one of the principal axes of the (coaxial) $\underline{\underline{g}}$-, $\underline{\underline{A}}$-, and $\underline{\underline{Q}}$ tensor (Figure 1e), eq 7 reduces to

$$\omega_{ENDOR} = |A_i/2 \pm \omega_I \bullet {}^3/_2Q_i| \quad (8)$$

According to eq 2, $4I$ ENDOR transitions are expected for a nucleus with arbitrary spin I. However, this assumes that the inhomogeneous broadening shifts the underlying spin packets in a way that the mw perturbation excites all ESR transitions, although each line in a different spin packet (see section IV). If the hyperfine structure is resolved in the ESR spectrum and each m_I state is affected individually by the mw driving field, either a four-line ENDOR spectrum (ESR observer, $-I < m_I < I$), or a two-line spectrum (ESR observer, $m_I = \pm I$) is observed. In cases where hyperfine and nuclear quadrupole interactions are of the same order of magnitude ($\mathcal{H}_{HFS} \approx \mathcal{H}_Q$), the interpretation of the ENDOR frequencies becomes more complex.[49]

In some spin systems, the observation of overtone transitions ($\Delta m_I \geq 2$)[50,51] and of multiple quantum transitions[52] have been reported. In the latter case two rf quanta of the same or of two different frequencies are simultaneously absorbed. A further contribution to the first-order ENDOR frequencies may arise from the direct dipole–dipole coupling between two nuclei. Such interactions are sometimes observed between adjacent protons of water molecules or methylene groups.[53]

Second-order contributions to the ENDOR transition frequencies are of the order of $A^2/\beta_e g B_0$ and cause shifts and splittings of the ENDOR lines.[4,48] For hyperfine couplings <10 MHz, these contributions are smaller than 10 kHz and are often neglected. For larger hyperfine couplings, however, second-order effects can become important and should be considered in the evaluation of the interaction tensors. In the case of two magnetically equivalent nitrogens directly coordinated to the metal ion in copper complexes, for example, each of the four ENDOR lines (eq 7) is split into a doublet by 200–300 kHz (Figure 1f).[54] In ENDOR experiments on transition metal ions, second order shifts may amount up to several megahertz.[55–57]

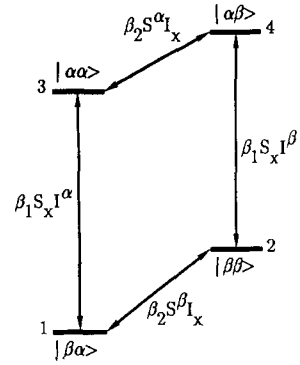

Figure 2. Energy level scheme of an isotropic $S = {}^1/_2$, $I = {}^1/_2$ spin system, $|a/2| < |\omega_I|$. ESR transitions, $|\alpha\alpha\rangle \leftrightarrow |\beta\alpha\rangle$ and $|\alpha\beta\rangle \leftrightarrow |\beta\beta\rangle$, and NMR transitions $|\alpha\alpha\rangle \leftrightarrow |\alpha\beta\rangle$ and $|\beta\alpha\rangle \leftrightarrow |\beta\beta\rangle$, are denoted by the corresponding terms in the Hamiltonian describing the interaction of the spins with selective mw and rf pulses, respectively.

III. Operator Formalism for the Description of Pulsed ENDOR Experiments

In this section we develop the mathematical machinery for the description of pulsed ENDOR experiments. The theory, which has become very popular in NMR, is only given to the extent that is necessary for the understanding of the basic principles of the experiments. For a more detailed description of the formalism, the reader is referred to the literature.[58,59]

The behavior of a spin system under a Hamiltonian $\mathcal{H}$ is described by the time evolution of the density operator σ defined by the Liouville–von Neumann equation

$$\dot{\sigma} = -i[\mathcal{H}, \sigma] \quad (9)$$

Assuming a time-independent Hamiltonian, the solution of eq 9 takes the form

$$\sigma(t) = R\sigma(0)R^{-1} = \exp\{-i\mathcal{H}t\}\sigma(0)\exp\{i\mathcal{H}t\} \quad (10)$$

or in shorthand notation

$$\sigma(0) \xrightarrow{\mathcal{H}t} \sigma(t) \quad (11)$$

The propagator $R = e^{-i\mathcal{H}t}$ (unitary operator $R^{-1} = R^\dagger$) is formulated according to the relevant Hamiltonian $\mathcal{H}$ operating during time t.

The form of $\mathcal{H}$ depends upon whether a mw pulse, an rf pulse, or a free precession period is considered. To present the basic concepts of the various pulsed ENDOR schemes in a straight forward and transparent way, we replace the internal Hamiltonian given in eq 1 by truncated Hamiltonians. For the description of most of the ENDOR schemes an isotropic $S = {}^1/_2$, $I = {}^1/_2$ electron–nuclear spin system represented by the Hamiltonian

$$\mathcal{H}_0 = \omega_S S_z + \omega_I I_z + a(S_z I_z + S_x I_x + S_y I_y) \quad (12)$$

is adequate. The corresponding four-level diagram is shown in Figure 2. In eq 12, $\omega_S = g_e\beta_e B_0/\hbar$ is the electron Zeeman frequency and $a(S_x I_x + S_y I_y)$ denotes the nonsecular part of the hyperfine coupling that is responsible for the second order frequency shifts mentioned in section II.

In the following, we assume that $\omega_S \gg a$ (high-field approximation). Since in this approximation, product base and eigenbase deviate only slightly from each other, the nonsecular contribution may be neglected

during free evolution under $\mathcal{H}_0$. This drastically simplifies the description of pulsed ENDOR experiments, without substantially affecting the final results. During evolution under an rf perturbation, however, nonsecular contributions become significant, since only a small change in the base functions may remarkably alter the transition matrix elements and, thus, the flip angle of the rf pulse (see below).

The Hamiltonians representing mw and rf pulses are time-dependent. This time dependence is removed by a transformation into a doubly rotating frame by the propagator

$$T = \exp\{-i(\omega_{mw}tS_z + \omega_{rf}tI_z)\} \quad (13)$$

where ω_{mw} and ω_{rf} denote the angular frequencies of the mw and the rf field, respectively. In the new frame, the internal high-field Hamiltonian reduces to

$$\mathcal{H}_0 = \Omega_S S_z + \Omega_I I_z + aS_zI_z \quad (14)$$

with $\Omega_S = \omega_S - \omega_{mw}$ and $\Omega_I = \omega_I - \omega_{rf}$. In the following, this Hamiltonian is used for the description of pulsed ENDOR experiments where only nuclear *single* quantum transitions are of interest. For pulsed ENDOR schemes where nuclear *multiple* quantum transitions play a dominant role, the three-spin system $S = {}^1/_2$, $I_1 = {}^1/_2$, $I_2 = {}^1/_2$, represented by the doubly rotating frame Hamiltonian

$$\mathcal{H}_0 = \Omega_S S_z + \Omega_{I1} I_{1z} + \Omega_{I2} I_{2z} + a_1 S_z I_{1z} + a_2 S_z I_{2z} \quad (15)$$

is applied.

We now move on to the description of the mw and rf pulses. The Hamiltonian during the application of a mw pulse is given by

$$\mathcal{H}_1 = \mathcal{H}_0 + \omega_1 S_x \quad (16)$$

The second term in eq 16 describes a pulse with a mw field strength (in angular frequencies) of $\omega_1 = g_e\beta_e B_1/\hbar = -\gamma_e B_1$ applied along the x axis of the rotating frame (x pulse), with B_1 denoting the amplitude of the circularly polarized mw field component (in tesla). For both, mw and rf pulses, we consistently use positive rotations in the right-handed sense. A pulse "applied along the x axis" then means that the axis of the Larmor frequency vector ω_L points to the positive x axis. For electrons ($\gamma_e < 0$), $\omega_L = \omega_1$ and $\mathbf{B}_1$ are parallel, for protons ($\gamma_p > 0$), the two vectors are antiparallel.[59]

A mw pulse is considered to be nonselective, when its field strength is much larger than the hyperfine interaction, $|\omega_1| \gg |a|$; i.e., all ESR transitions within a spin packet are simultaneously excited by a strong pulse of short duration. With this condition, $\omega_1 S_x$ is the dominant term in eq 16 and the internal Hamiltonian $\mathcal{H}_0$ can be neglected during the pulse.

On the other hand, a mw pulse is considered to be selective, if it only affects a single ESR line. To describe such line-selective pulses, which fulfil the condition $|\omega_1| \ll |a|$, we first rearrange eq 16 with $\mathcal{H}_0$ of eq 14 to give

$$\mathcal{H}_1 = [\Omega_S + (a/2)]S_zI^\alpha + [\Omega_S - (a/2)]S_zI^\beta + \omega_1 S_xI^\alpha + \omega_1 S_xI^\beta + \Omega_I I_z \quad (17)$$

In eq 17, I^α and I^β denote nuclear spin polarization operators[60-62] that select the ESR line associated with the α and β nuclear spin state, respectively

$$I^\alpha = {}^1/_2\,\hat{I} + I_z \quad (18a)$$

$$I^\beta = {}^1/_2\,\hat{I} - I_z \quad (18b)$$

with the complementary formulae

$$\hat{I} = I^\alpha + I^\beta \quad (19a)$$

$$I_z = {}^1/_2(I^\alpha - I^\beta) \quad (19b)$$

and $\hat{I}$ being the unity operator.

The spin operators $S_xI^\alpha = S_x^{(13)}$ and $S_xI^\beta = S_x^{(24)}$ in eq 17 (with $S_xI^\alpha + S_xI^\beta = S_x$) are called single-transition operators.[59] Generally, a single-transition operator $S^{(rs)}$ refers to the transition between two energy levels $|r\rangle$ and $|s\rangle$. All the other energy levels are disregarded and the subsystem is treated as a virtual two-level system. In our two-spin systems, S_xI^α and S_xI^β refer to the (allowed) ESR transitions between the states $|\alpha\alpha\rangle \leftrightarrow |\beta\alpha\rangle$ and $|\alpha\beta\rangle \leftrightarrow |\beta\beta\rangle$, respectively. Correspondingly the single-transition operators $S^\alpha I_x = I_x^{(34)}$ and $S^\beta I_x = I_x^{(12)}$, with the electron spin polarization operators S^α and S^β, selecting NMR lines associated with the α and β electron spin state, refer to the NMR transitions $|\alpha\alpha\rangle \leftrightarrow |\alpha\beta\rangle$ and $|\beta\alpha\rangle \leftrightarrow |\beta\beta\rangle$. In the following we will always explicitly write a single-transition operator as the product of a polarization operator and an angular momentum operator, since with this notation it is especially easy to follow the evolution of the spin system. The same notation is also used to assign the transitions in the four-level scheme in Figure 2.

We now discuss eq 17 in more detail. For a mw pulse on-resonance with transition $|\alpha\alpha\rangle \leftrightarrow |\beta\alpha\rangle$, $\Omega_S = \omega_S - \omega_{mw} = -a/2$, the first term in eq 17 reduces to zero, whereas the second term becomes $-aS_zI^\beta$. For a line-selective pulse with $|\omega_1| \ll |a|$, transition $|\alpha\beta\rangle \leftrightarrow |\beta\beta\rangle$ is far off-resonance, so that the term $\omega_1 S_xI^\beta$ can be ignored. From the three commuting terms $\omega_1 S_xI^\alpha$, $-aS_zI^\beta$, and $\Omega_I I_z$ only the first one is of importance for the description of selective pulses in polarization transfer ENDOR. The other two terms commute with S_z and have only to be considered in coherence transfer ENDOR experiments. A corresponding situation holds for a mw pulse on-resonance with transition $|\alpha\beta\rangle \leftrightarrow |\beta\beta\rangle$. The rotating frame Hamiltonians for selective mw x pulses acting on transition $|\alpha\alpha\rangle \leftrightarrow |\beta\alpha\rangle$ or $|\alpha\beta\rangle \leftrightarrow |\beta\beta\rangle$ can then be described by

$$\mathcal{H}_1^\alpha = \omega_1 S_xI^\alpha \quad (20)$$

and

$$\mathcal{H}_1^\beta = \omega_1 S_xI^\beta \quad (21)$$

respectively.

For both, selective and nonselective mw excitation, a pulse of duration t_{mw} and amplitude ω_1 results in a nominal (on-resonance) flip angle $\beta_1 = \omega_1 t_{mw} = -\gamma_e B_1 t_{mw}$. Note that in a system with an anisotropic $\underline{\mathbf{g}}$ tensor, β_1 depends on the effective gyromagnetic ratio defined by $\gamma_{eff} = -\beta_e g_{eff}(\varphi,\theta)/\hbar$, where φ and θ are the polar angles describing the orientation of $\mathbf{B}_0$ in the molecular frame.

Nonselective and selective rf pulses are formulated in a similar way. The rotating frame Hamiltonian for a nonselective rf x pulse is given by

$$\mathcal{H}_2 = -\gamma_n B_2 I_x - \gamma_e B_2 S_x \quad (22)$$

where $-\gamma_n B_2 = -g_n\beta_n B_2/\hbar = \omega_2$ is the strength of the external rf field in angular frequency units and B_2 is the amplitude of the circularly polarized rf field component. The second term in eq 22 describes the interaction of the rf field with the electron spin and contributes only

in the first-order spin base to the nuclear transition elements. The change of these transition elements by the electron spin is "called hyperfine enhancement",[63] because it is the hyperfine coupling (namely the nonsecular term) that is responsible for the state mixing. Although, the difference between product base and eigenbase is small at high B_0 fields, the contribution of the second term in eq 22 can be significant (note that for protons, $\gamma_e/\gamma_n = 658$).

The hyperfine enhancement can be described classically as originating from a modulation of the internal magnetic field produced by the electron spin at the nucleus with frequency ω_{rf}. The resulting driving field which induces nuclear transitions is then the sum of the external rf field and the oscillating component of the internal field. For an isotropic hyperfine interaction, the field acting on the nucleus is given by

$$B_2^E = EB_2 = |1 + (m_S a/\omega_I)|B_2 \qquad (23)$$

The hyperfine enhancement factor E depends on m_S, ω_I, and the sign and the magnitude of the isotropic hyperfine coupling constant a. It manifests itself either in an increase or a decrease of the field amplitude of B_2. Analytical expressions for enhancement factors of anisotropic spin systems have been given elsewhere.[4]

The Hamiltonian in eq 22 can be transformed into a frame in which the representation of $\mathcal{H}_0$ is diagonal. By neglecting transition matrix elements which induce ESR transitions with a driving frequency far off-resonance ($\omega_{rf} \ll \omega_S$), the Hamiltonian during a nonselective rf pulse reduces to

$$\mathcal{H}_2 = \omega_2^E I_x \qquad (24)$$

with the hyperfine enhanced rf field strength $\omega_2^E = -\gamma_n EB_2$.

Correspondingly, rf x pulses acting selectively on the nuclear transition in the $m_S = {}^1/_2$ and $m_S = -{}^1/_2$ electron spin manifold, respectively, are represented by

$$\mathcal{H}_2^\alpha = \omega_2^E S^\alpha I_x \qquad (25a)$$

and

$$\mathcal{H}_2^\beta = \omega_2^E S^\beta I_x \qquad (25b)$$

The nominal flip angle for selective or nonselective rf pulses is then defined by $\beta_2^E = \omega_2^E t_{rf}$. (In the following, we drop the superscipt E, except in cases where it is necessary for clarity.)

In all pulsed ENDOR experiments discussed in this work, the doubly rotating frame Hamiltonian is piecewise constant and time-independent and can be divided into n periods. The density operator at the end of the sequence is given by

$$\sigma(0) \xrightarrow{\mathcal{H}^{(1)}\tau_1} \sigma(\tau_1) \xrightarrow{\mathcal{H}^{(2)}\tau_2} \sigma(\tau_1 + \tau_2) \ldots \xrightarrow{\mathcal{H}^{(n)}\tau_n} \sigma(\sum_n \tau_n) \qquad (26)$$

The observable magnetization components of the electron spin at time $t = \sum \tau_n$ along the x and y axis of the rotating frame can be evaluated from the trace relations

$$M_x(t) = \mathrm{Tr}\{\sigma(t)S_x\} \qquad (27a)$$

and

$$M_y(t) = \mathrm{Tr}\{\sigma(t)S_y\} \qquad (27b)$$

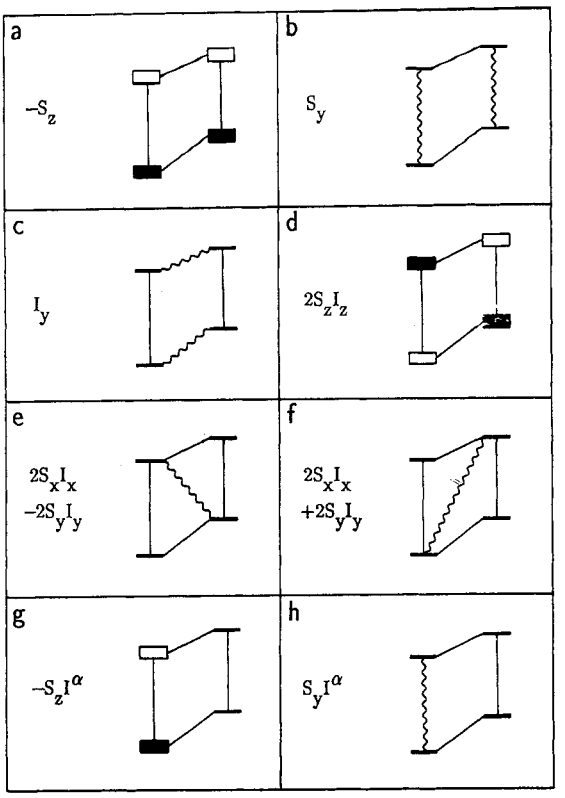

Figure 3. Graphical representations of product operators in a $S = {}^1/_2, I = {}^1/_2$ spin system. Empty and full energy levels mark populations of states that are depleted or more populated, respectively, than in the demagnetized state (marked by a line). Coherences are represented by wavy lines: (a) electron spin polarization, (b) electron spin coherence, (c) nuclear spin coherence, (d) longitudinal electron–nuclear two-spin order, (e) double-quantum coherence, (f) zero-quantum coherence, (g) spin polarization of one ESR transition, and (h) spin coherence of one ESR transition.

respectively.

Application of the density operator formalism based on eq 9 is straight forward but often rather cumbersome. Moreover, an explicit matrix calculation provides little physical insight into the workings of the experiments. An alternative approach that combines computational convenience with physical transparency is to express the density operator $\sigma(t)$ as a linear combination of base operators[58]

$$\sigma(t) = \sum_n b_n(t)B_n \qquad (28)$$

with B_n denoting Cartesian product operators. In the case of our electron–nuclear two-spin system, the complete base set $\{B_n\}$ consists of the 16 orthogonal product operators

$$\tfrac{1}{2}\hat{I}_S\hat{I}_I \quad S_x, S_y, S_z, I_x, I_y, I_z \quad 2S_xI_x, 2S_xI_y, 2S_xI_z$$
$$2S_yI_x, 2S_yI_y, 2S_yI_z \quad 2S_zI_x, 2S_zI_y, 2S_zI_z$$

The unity operators $\hat{I}_S$ and $\hat{I}_I$ are left out in the product operator notation (e.g. $S_x\hat{I}_I = S_x$).

Each product operator has its specific physical meaning. In the following, we adapt the nomenclature used in NMR[58] to electron-nuclear spin systems. Corresponding pictorial representations of some of the product operators in the energy level diagram are shown in Figure 3.

S_z (=S_zI^α + S_zI^β) equal electron spin polarization across both ESR transitions

S_x, S_y in-phase electron spin coherence (both ESR transitions have the same transverse magnetization along the x or y axis of the rotating frame, respectively.)

I_z equal nuclear spin polarization across both NMR transitions

I_x, I_y in-phase nuclear spin coherence

$2S_zI_z$ (=S_zI^α − S_zI^β) longitudinal electron–nuclear two-spin order (The two ESR and the two NMR transitions are polarized. In this spin-correlated population of the energy levels, there is no net polarization.)

$2S_xI_z$, $2S_yI_z$ antiphase electron spin coherence (The two individual components are opposite in phase. Antiphase magnetization has zero integrated intensity.)

$2S_zI_x$, $2S_zI_y$ antiphase nuclear spin coherence

$2S_xI_x$, $2S_yI_y$, $2S_xI_y$, $2S_yI_x$ electron-nuclear two-spin coherence (These two-spin coherences represent a superposition of electron–nuclear zero and double quantum coherences (forbidden ESR transitions). For example: $2S_xI_x + 2S_yI_y$ represents pure zero quantum coherence, $2S_xI_x - 2S_yI_y$ represents pure double quantum coherence.)

Also linear combinations of product operators have a simple physical meaning.

S_xI^α (=$^1/_2S_x + S_xI_z$), S_yI^α, S_xI^β, S_yI^β spin coherence of one ESR transition

S_zI^α, S_zI^β spin polarization of one ESR transition

$S^\alpha I_x$, $S^\alpha I_y$, $S^\beta I_x$, $S^\beta I_y$ spin coherence of one NMR transition

$S^\alpha I_z$, $S^\beta I_z$ spin polarization of one NMR transition

The evolution of any individual product operator B_n under a Hamiltonian represented by another product operator B_m, can be expressed by[62]

$$\exp\{-i\varphi B_m\}B_n \exp\{i\varphi B_m\} = B_n \cos\varphi - i[B_m, B_n] \sin\varphi \quad (29a)$$

or

$$B_n \xrightarrow{\varphi B_m} B_n \cos\varphi - i[B_m,B_n] \sin\varphi \quad (29b)$$

where φB_m is a term in the internal Hamiltonian or a Hamiltonian that represents a mw or rf pulse. The transformations relevant for the pulsed ENDOR experiments are collected in Table I. With the aid of this dictionary we are in a position to describe all ENDOR methods in an elegant way, just by using these transformations or obvious variations of it in a chronological sequence according to the pulse schemes.

IV. Polarization Transfer ENDOR

In a polarization transfer pulsed ENDOR experiment only polarizations are involved in the transfer of magnetization between electron and nuclear spins. A polarization transfer ENDOR scheme can be divided into three time intervals, a preparation period, a mixing period, and a detection period as is shown in Figure 4.

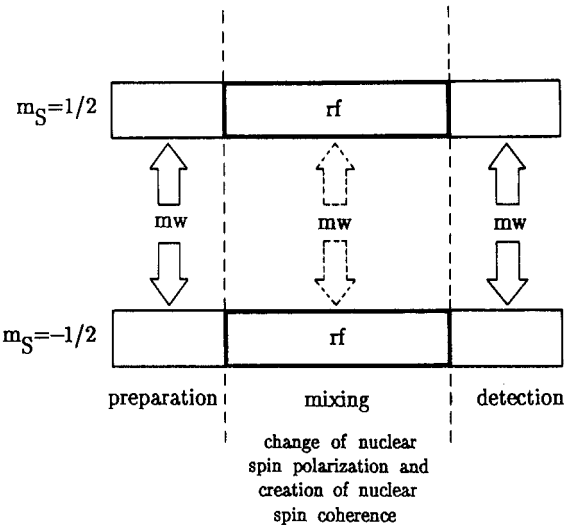

Figure 4. Subdivision of a polarization transfer ENDOR experiment into a preparation, mixing, and detection period.

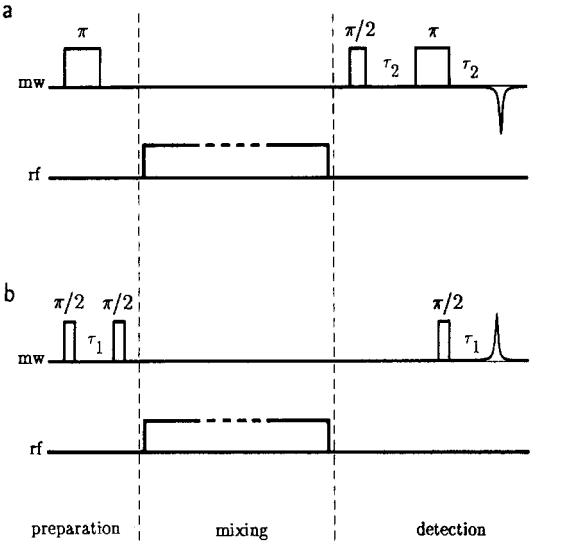

Figure 5. Basic mw pulse schemes used in polarization transfer ENDOR experiments: (a) selective mw pulses, and (b) nonselective mw pulses.

During the preparation period nuclear spin polarization is created. In the following mixing period rf irradiation changes this nuclear spin polarization and creates nuclear spin coherence. In some experiments, also mw pulses are applied during the mixing period to exchange polarization between the two electron spin states. During the detection period, the changes of the electron spin polarization caused by the rf perturbation are recorded via an electron spin echo.

A. Basic Microwave Pulse Schemes

Two basic mw pulse sequences are commonly used in pulsed ENDOR experiments. They represent the limiting cases for selective mw pulse excitation (Figure 5a) and for nonselective excitation (Figure 5b). In this subsection, we follow for these two cases the evolution of a particular spin packet; the inhomogeneity of the ESR lines is introduced later.

1. Selective Preparation and Detection

A pulsed ENDOR experiment starts with the equilibrium state that is described by the density operator $\sigma(0) \propto -S_z$ (Figure 3a). In this expression, we omitted

TABLE I. Collection of Formulas for the Transformation of Product and Single Transition Operators

Electron Zeeman Interaction[a]

I $S_z \xrightarrow{\Omega_S t S_z} S_z$

IIa $S_x \xrightarrow{\Omega_S t S_z} S_x \cos(\Omega_S t) + S_y \sin(\Omega_S t)$

IIb $S_y \xrightarrow{\Omega_S t S_z} S_y \cos(\Omega_S t) - S_x \sin(\Omega_S t)$

III $2S_yI_z \xrightarrow{\Omega_S t S_z} 2S_yI_z \cos(\Omega_S t) - 2S_xI_z \sin(\Omega_S t)$

Hyperfine Interaction

IV $S_z \xrightarrow{[(a/2)t][2S_zI_z]} S_z$

Va $S_x \xrightarrow{[(a/2)t][2S_zI_z]} S_x \cos[(a/2)t] + 2S_yI_z \sin[(a/2)t]$

Vb $S_y \xrightarrow{[(a/2)t][2S_zI_z]} S_y \cos[(a/2)t] - 2S_xI_z \sin[(a/2)t]$

VIa $2S_xI_z \xrightarrow{[(a/2)t][2S_zI_z]} 2S_xI_z \cos[(a/2)t] + S_y \sin[(a/2)t]$

VIb $2S_yI_z \xrightarrow{[(a/2)t][2S_zI_z]} 2S_yI_z \cos[(a/2)t] - S_x \sin[(a/2)t]$

VIIa $2S_xI_x \xrightarrow{[(a/2)t][2S_zI_z]} 2S_xI_x$

VIIb $2S_xI_y \xrightarrow{[(a/2)t][2S_zI_z]} 2S_xI_y$

Nonselective Mw Pulse[b]

VIIIa $S_z \xrightarrow{\beta S_x} S_z \cos\beta - S_y \sin\beta$

VIIIb $S_y \xrightarrow{\beta S_x} S_y \cos\beta + S_z \sin\beta$

IX $2S_zI_z \xrightarrow{\beta S_x} 2S_zI_z \cos\beta - 2S_yI_z \sin\beta$

Selective Mw Pulse[b]

Xa $S_zI^\alpha \xrightarrow{\beta S_xI^\alpha} S_zI^\alpha \cos\beta - S_yI^\alpha \sin\beta$

Xb $S_yI^\alpha \xrightarrow{\beta S_xI^\alpha} S_yI^\alpha \cos\beta + S_zI^\alpha \sin\beta$

XI $S_zI^\beta \xrightarrow{\beta S_xI^\alpha} S_zI^\beta$

Useful Transcriptions

XII $\xrightarrow{\beta S_\phi} = \xrightarrow{-\phi S_z} \xrightarrow{\beta S_x} \xrightarrow{\phi S_z}$

XIII $\xrightarrow{\beta S_xI^\alpha} = \xrightarrow{(\beta/2)S_x} \xrightarrow{(\beta/2)2S_xI_z}$

XIV $\xrightarrow{(\beta/2)2S_xI_z} = \xrightarrow{(-\pi/2)S_y} \xrightarrow{(\beta/2)2S_xI_z} \xrightarrow{(\pi/2)S_y}$

[a] For nuclear Zeeman interaction interchange S and I. [b] For an rf pulse, interchange S and I.

the term with the unity operator ($\hat{1}$ is invariant to transformations), used the high-temperature approximation, and deleted the constant factor in front of the operator S_z.[62] Population differences between the nuclear spin states within a m_S manifold are considered to be negligibly small.

Application of a selective mw x pulse with flip angle π on-resonance with ESR transition $|\alpha\alpha\rangle \leftrightarrow |\beta\alpha\rangle$ causes the transformation

$$-S_z = -S_zI^\alpha - S_zI^\beta \xrightarrow{\pi S_xI^\alpha} S_zI^\alpha - S_zI^\beta = 2S_zI_z = \sigma_{prep}^{sel} \quad (30)$$

The result of eq 30 is obtained by using transformation X and XI in Table I. For the convenience of the reader, we will always refer in the description of a pulse experiment to some of the more important transformation formulae collected in this table.

The selective mw pulse with flip angle $\beta_1 = \pi$ converts the electron spin polarization $-S_z$ into *electron–nuclear two-spin order* $2S_zI_z$ (Figure 3d), i.e. the nuclear spins in both NMR transitions are now polarized. This creation of nuclear spin polarization is a prerequisite for all the ENDOR experiments based on the transfer of polarization. After a mixing time T, the detection sequence $\pi/2$–τ_2–π–τ_2 again with selective mw pulses is used to probe the electron spin polarization of transition $|\alpha\alpha\rangle \leftrightarrow |\beta\alpha\rangle$ via a two-pulse echo that is created at time $T + 2\tau_2$ (X,II,III,V,VI):

$$\sigma_{prep}^{sel} \xrightarrow{(\pi/2)S_xI^\alpha} -S_yI^\alpha - S_zI^\beta \quad (31)$$

$$\xrightarrow{\mathcal{H}_0\tau_2} \xrightarrow{\pi S_xI^\alpha} \xrightarrow{\mathcal{H}_0\tau_2} S_yI^\alpha - S_zI^\beta = \sigma_{echo}^{sel}$$

2. Nonselective Preparation and Detection

Electron-nuclear two-spin order $2S_zI_z$ can also be created with *nonselective* mw pulses, provided that a time interval is introduced during which the spin system can evolve under a hyperfine interaction. This is achieved, for example, by the preparation sequence $\pi/2$–τ_1–$\pi/2$ (Figure 5b) that consists of two nonselective $\pi/2$ pulses separated by the time τ_1 (VIII,II,V):

$$-S_z \xrightarrow{(\pi/2)S_x} S_y \xrightarrow{\mathcal{H}_0\tau_1} \xrightarrow{(\pi/2)S_x}$$
$$S_z \cos[(a/2)\tau_1] \cos(\Omega_S\tau_1) =$$
$$2S_zI_z \sin[(a/2)\tau_1] \sin(\Omega_S\tau_1) = \sigma_{prep}^{nonsel} \quad (32)$$

In the expression for σ_{prep}^{nonsel}, only the two terms that contribute to the echo at the end of the sequence have been considered. Both of them are functions of the hyperfine coupling constant a and the resonance offset Ω_S. Note that two-spin order is only created if $a \neq 0$ and if the frequency of the mw pulse does not coincide with electron Zeeman frequency ($\Omega_S = 0$).

The nonselective $\pi/2$ detection pulse applied after the mixing time T, creates a stimulated echo at time $T + 2\tau_1$, (IX,VI,II):

$$\sigma_{prep}^{nonsel} \xrightarrow{(\pi/2)S_x} \xrightarrow{\mathcal{H}_0\tau_1}$$
$$-S_y[\tfrac{1}{2}[1 + \cos(a\tau_1) \cos(2\Omega_S\tau_1)]] = \sigma_{echo}^{nonsel} \quad (33)$$

B. Standard Polarization Transfer ENDOR Schemes

In the following, we discuss the different polarization transfer ENDOR experiments introduced in the literature up to now. With a few exceptions, they all make use of the two basic mw pulse schemes for preparation and detection and differ only in the pulse sequences applied during the mixing period.

1. Davies-ENDOR

The pulsed ENDOR scheme introduced by Davies[13] is based on selective mw pulses (Figure 5a). During the mixing period, a selective rf pulse with flip angle β_2 is applied. On-resonance, with one of the nuclear tran-

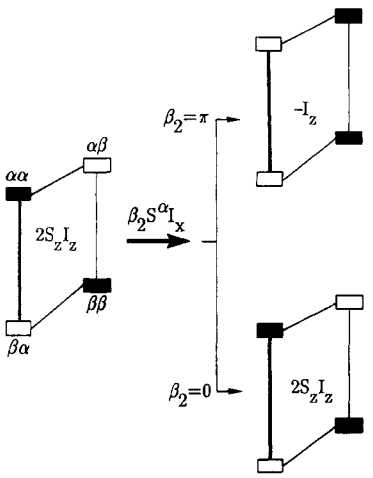

Figure 6. Effect of an rf pulse on-resonance with the nuclear transition $|\alpha\alpha\rangle \leftrightarrow |\alpha\beta\rangle$ on the populations of the energy levels in a Davies-ENDOR experiment. The ESR transition, $|\alpha\alpha\rangle \leftrightarrow |\beta\alpha\rangle$, used for preparation and detection, is marked by an intense line.

sitions, e.g. with transition $|\alpha\alpha\rangle \leftrightarrow |\alpha\beta\rangle$, the rf pulse changes the density operator σ^{sel}_{prep} in eq 30 to (X):

$$\sigma^{sel}_{prep} = 2S_zI_z \xrightarrow{\beta_2 S^\alpha I_x} (S_zI^\alpha - S_zI^\beta)[\tfrac{1}{2}(1 + \cos\beta_2)] - I_z[\tfrac{1}{2}(1 - \cos\beta_2)] - S^\alpha I_y \sin\beta_2 = \sigma^{sel}_{mix} \quad (34)$$

Figure 6 shows the corresponding populations before and after the mixing period with $\beta_2 = 0$ and π.

The detection sequence with mw pulses selectively acting on the same ESR transition as the preparation pulse, creates from the S_zI^α term a two-pulse echo at time $T + 2\tau_2$ (V):

$$\sigma^{sel}_{mix} = S_zI^\alpha[\tfrac{1}{2}(1 + \cos\beta_2)] \xrightarrow{(\pi/2)S_xI^\alpha} \xrightarrow{\mathcal{H}_0\tau_2} \xrightarrow{\pi S_xI^\alpha} \xrightarrow{\mathcal{H}_0\tau_2} S_yI^\alpha[\tfrac{1}{2}(1 + \cos\beta_2)] = \sigma^{sel}_{echo} \quad (35)$$

Up to now, we have only considered a single spin packet consisting of two ESR transitions split by the hyperfine coupling constant a. However, due to g-strain effects[64] and the large number of unresolved hyperfine couplings present in the solid state, the ESR lines are usually inhomogeneously broadened. We therefore briefly discuss the consequences of these broadening mechanisms for the Davies-ENDOR experiment, assuming that the inhomogeneity is accomplished by a spread of identical spin packets.

For an inhomogeneous line width small compared to the hyperfine splitting a, $\Gamma_{inh} \ll a$, each of the two ESR transitions can be excited separately with selective mw pulses. Equation 35 then describes the Davies-ENDOR experiment adequately. Since in this case the hyperfine splitting is also resolved in the ESR spectrum, there is usually no need to record an ENDOR spectrum, except for the determination of quadrupole coupling constants of nuclei with $I \geq 1$.

In most spin systems, however, the inhomogeneity is much larger than the hyperfine couplings of interest, $\Gamma_{inh} \gg a$. For this situation, the influence of the Davies-ENDOR sequence on the ESR line shape is shown in Figure 7. In these figures a line shape function $g(\Omega_S) = 1 = I_{ESR}$ ($\Gamma_{inh} = \infty$) is assumed and off-resonance effects are neglected. Prior to the application of the first mw pulse, two spin packets shifted by the hyperfine coupling constant a contribute to each field position of the ESR signal, the high-field line of one spin packet

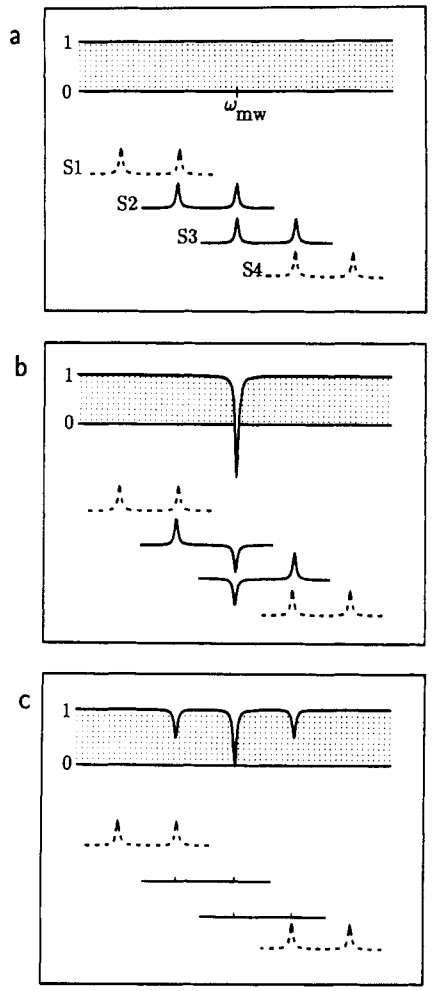

Figure 7. Influence of the Davies pulse sequence on an inhomogeneously broadened ESR line ($\Gamma_{inh} = \infty$): (a) equilibrium state, ESR line shape, and polarization of four selected spin packets (marked by S1, S2, S3 and S4); (b) situation after the selective mw pulse with frequency ω_{mw}; and (c) situation after the selective rf pulse on-resonance with one of the NMR transitions.

and the low-field line of an other spin packet. The behavior of four such spin packets (marked by S1, S2, S3, and S4) is considered in more detail. The selective mw π-pulse inverts the population of transition $|\alpha\alpha\rangle \leftrightarrow |\beta\alpha\rangle$ in S2 and transition $|\alpha\beta\rangle \leftrightarrow |\beta\beta\rangle$ in S3, resulting in a hole in the ESR line with intensity $I_{ESR} = -1$. The selective rf π-pulse on-resonance either with ENDOR transition $|\alpha\alpha\rangle \leftrightarrow |\alpha\beta\rangle$ or $|\beta\alpha\rangle \leftrightarrow |\beta\beta\rangle$ inverts the corresponding nuclear polarizations and, thus, removes the electron spin polarization of S2 and S3 (see also Figure 6). The original ESR line is now perturbed by three holes, the center hole with an ESR signal intensity $I_{ESR} = 0$ and two side holes with intensity $I_{ESR} = {}^1/_2$, each, shifted from the center hole by the hyperfine coupling constant a. The two remaining side hole intensities are caused by the spin packets S1 and S4 that are not affected by the mw and rf pulses.

In the Davies-ENDOR experiment, the intensity change of the *center hole* is observed as a function of the radiofrequency. With σ^{sel}_{echo} from eq 35, the relative echo intensity for S2 at time $T + 2\tau_2$ is then calculated to

$$I^{sel}_{echo}(\beta_2) = \mathrm{Tr}\{\sigma^{sel}_{echo}(-S_y)\} = -\tfrac{1}{4}(1 + \cos\beta_2) \quad (36)$$

with $-S_y$ denoting the detection operator. A corresponding expression holds for spin packet S3. (To get

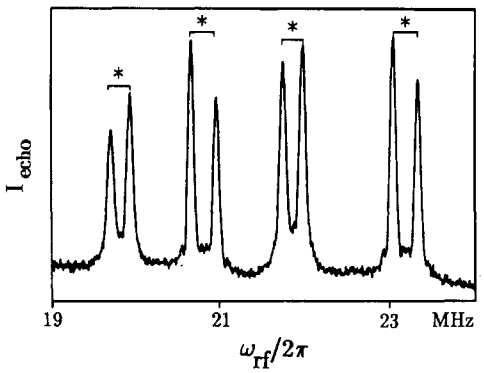

Figure 8. Single-crystal Davies-ENDOR spectrum of the two magnetically equivalent nitrogens of Cu(II)(salicylaldoxime) diluted in a single crystal of the corresponding nickel complex: mw pulse lengths, t^{π}_{mw} = 100 ns, $t^{\pi/2}_{mw}$ = 100 ns, t^{π}_{mw} = 200 ns, t_{rf} = 12.5 μs; arbitrary orientation of the crystal; temperature, 10 K; second-order splittings are marked by *.

a positive two-pulse echo signal, the detection operator has to be chosen along the $-y$ axis). The amplitude of I^{sel}_{echo} is maximum for $\beta_2 = 0$ ($|I^{sel}_{echo}(0)| = {}^1/_2$), and minimum for $\beta_2 = \pi$ ($I^{sel}_{echo}(\pi) = 0$). This change in echo intensity induced by the rf pulse can be expressed in terms of an ENDOR efficiency defined by[35]

$$F_{ENDOR} = \tfrac{1}{2}|[I_{echo}(\text{rf off}) - I_{echo}(\text{rf on})]/I_{echo}(\text{rf off})| \quad (37)$$

which is a measure for the relative change of the echo amplitude under the rf pulse. According to this definition the ENDOR efficiency lies in the range $0 \leq F_{ENDOR} \leq 1$ where $F_{ENDOR} = 1$ (100%) corresponds to an inversion of the echo. In the Davies experiment with $\beta_2 = \pi$, F_{ENDOR} = 0.5 (50%). The same conclusion can also be reached by considering the population distribution shown in Figure 6: For $\beta_2 = \pi$ the population difference across the ESR transition $|\alpha\alpha\rangle \leftrightarrow |\beta\alpha\rangle$ vanishes, while it is maximum for $\beta_2 = 0$. (The ENDOR efficiency as defined in eq 37 should only be used for the description of experiments with ideal selective or nonselective pulses acting on one spin packet).

An illustrative example for a Davies–ENDOR spectrum is shown in Figure 8. In this single-crystal spectrum of a copper complex with two magnetically equivalent nitrogen nuclei,[65] each of the four nitrogen transitions is split into a doublet by about 300 kHz, due to second order contributions (cf. Figure 1f).

In the following, we discuss the influence of finite pulse lengths and of the hyperfine enhancement on the ENDOR spectrum. First the change of the inhomogeneously broadened ESR line shape caused by the mw and rf pulses of finite length is considered. Numerical simulations of the ESR line shape for two values of the product of the hyperfine coupling constant and the mw pulse length, at_{mw}, are shown in Figure 9, parts a and b. For $at_{mw}/2\pi > 1$, the mw pulse excites only one transition in each spin packet, whereas in the case of $at_{mw}/2\pi \lesssim 1$, the mw pulse affects both ESR transitions. Such a simultaneous excitation of two ESR transitions is sometimes called "self-ELDOR" (ELDOR: electron–electron double resonance), since two electron spin transitions with different frequencies are excited. In both cases, a hole at frequency ω_{mw} with a depth $I_{ESR} = -1$, a width $\Gamma_{hole} \propto 2\pi/t_{mw}$ and an off-resonance pattern typical for a pulse excitation with a nominal flip angle π is created (Figure 9, parts a and b, top). The

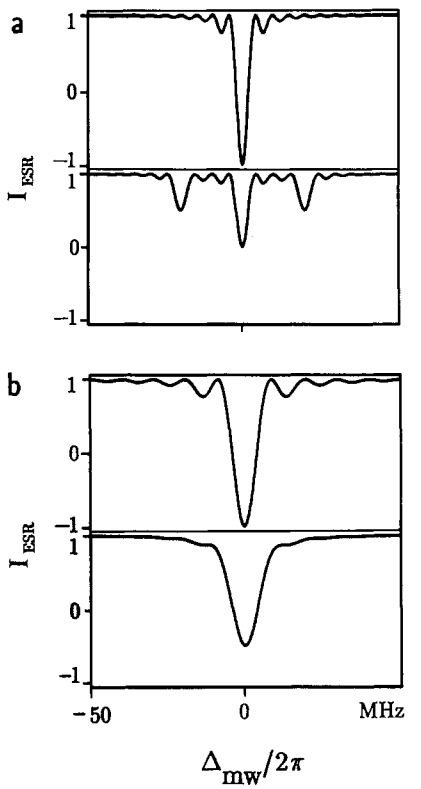

Figure 9. Numerical simulations of ESR line shapes in the Davies-ENDOR experiment for two values of the product at_{mw} (a, isotropioc hyperfine coupling constant; t_{mw}, mw pulse length) vs Δ_{mw} (Δ_{mw} = 0: on-resonance with one of the two ESR transitions): (a) $a/2\pi$ = 20 MHz, t_{mw} = 200 ns; $at_{mw}/2\pi$ = 4 (after the mw preparation pulse (top); after the rf pulse (bottom)). (b) $a/2\pi$ = 4 MHz, t_{mw} = 100 ns; $at_{mw}/2\pi$ = 0.4 (after the mw preparation pulse (top); after the rf pulse (bottom)).

rf pulse, applied on-resonant with one of the nuclear transition frequencies transfers part of the center hole to the two side holes, thereby reducing the depth of the center hole. For $at_{mw}/2\pi > 1$, this results in a hole intensity ratio of 1:2:1 (Figure 9a, bottom), whereas in the case with $at_{mw}/2\pi \lesssim 1$ the transfer of polarization by the rf pulse becomes incomplete, and center and side hole overlap (Figure 9b, bottom). The depth of the center hole is now recorded via a two-pulse electron spin echo.

Experimentally, it is most convenient to use the same field strength ω_1 for all three mw pulses in the preparation and detection period, with a duration of the π pulses twice as long as the one of the $\pi/2$ pulse. With this sequence the shape of the echo with and without an rf pulse looks quite irregular (Figure 10a). This is due to the fact that the frequency range excited by the detection sequence is comparable with the width of the center hole (for comparison, see in Figure 10a the echo shape obtained without the mw preparation pulse). These shapes of the electron spin echo could also be verified experimentally.[66]

If the two detection pulses are more selective than the preparation pulse, one monitors only that region of the center hole, which is relatively constant in amplitude. Consequently, the two-pulse echo with the typical bell-like shape of an echo obtained from a broad ESR line is fully inverted if a preparation pulse precedes (Figure 10b). With rf excitation, the whole echo intensity drops to zero. The absolute echo amplitude I_{echo} and the absolute ENDOR intensity, however, become

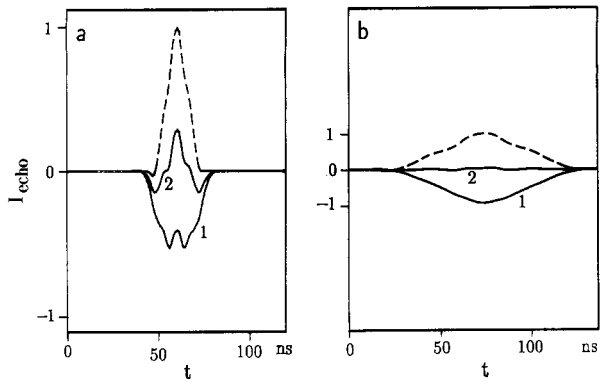

Figure 10. Simulated echo shapes in a Davies-ENDOR experiment for two sets of mw pulses and $\Gamma_{inh} = \infty$: 1, without rf pulse; 2, with rf pulse. The echo shapes obtained without a mw preparation pulse are marked by dashed lines. The absolute scaling of the echo intensity is the same in both figures: (a) All three pulses with lengths 200 ns, 100 ns, and 200 ns have the same mw field strength $\omega_1/2\pi = 2.5$ MHz. (b) The preparation pulse (length, 200 ns; $\omega_1/2\pi = 2.5$ MHz) is shorter (less selective) than the detection pulses (lengths, 400 ns and 800 ns; $\omega_1/2\pi = 0.625$ MHz).

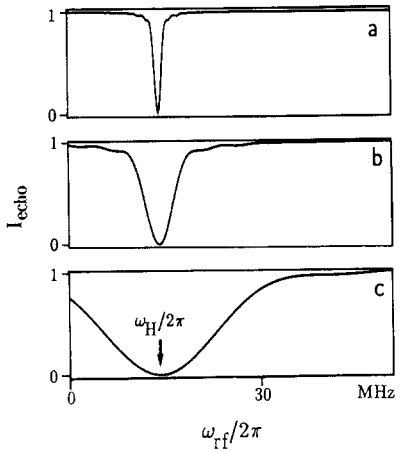

Figure 11. Effect of the mw pulse lengths in a Davies-ENDOR experiment (self-ELDOR hole) on the signal intensity of proton transitions ($2t^{\pi/2}_{mw} = t^{\pi}_{mw}$) (for all values of a, an rf flip angle of $\beta_2 = \pi$ is used): t^{π}_{mw} = (a) 400 ns; (b) 100 ns; and (c) 25 ns.

smaller with increasing selectivity of the mw pulses. It is important to note that, for the other extreme case of ideal *nonselective* mw detection pulses, the ENDOR effect on the echo maximum completely disappears. This is due to the fact that nonselective pulses measure only the net electron spin polarization which cannot be changed by an rf pulse.

We now return to the self-ELDOR effect. The influence of the mw pulse length on the peak intensity I_{echo} of a proton ENDOR line is shown in Figure 11 for three different t_{mw} values. According to this figure, the ENDOR efficiency is zero for $a = 0$ ($\omega_{rf} = \omega_H$), independent of the mw pulse length; i.e. weakly coupled protons giving rise to a strong matrix line in the cw ENDOR spectrum may not be observed in a Davies-ENDOR experiment. The width of the self-ELDOR hole (FWHH) that prevents ENDOR detection is given by $\Gamma_{ELDOR} \approx 2\pi/2t^{\pi}_{mw}$, where t^{π}_{mw} is the length of the preparation pulse.

The self-ELDOR effect can be used to assign ENDOR lines to corresponding nuclei.[38,66] This is demonstrated in Figure 12, which shows two ENDOR spectra of a copper complex.[66] They are recorded in the range 4 MHz $\leq \omega_{rf}/2\pi \leq$ 19 MHz with two different sets of mw pulse lengths and consist of a large number of

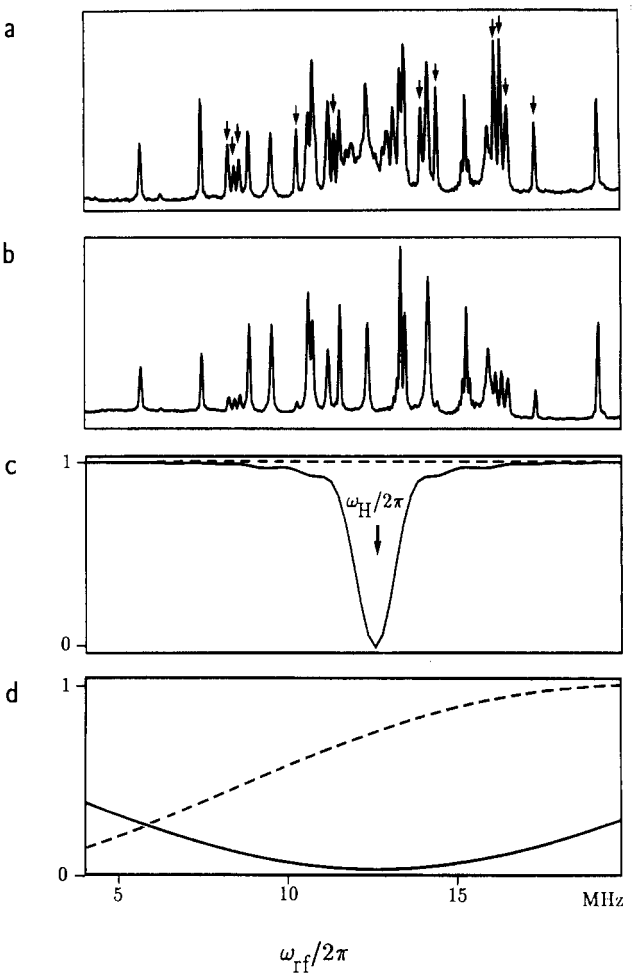

Figure 12. Single-crystal Davies-ENDOR spectra of Cu(II)-(bipyram)(dien), (bipyram = 2,2-bipyridylamine, dien = diethylenetriamine), diluted in a single crystal of the corresponding nickel complex for two sets of mw pulse lengths, arbitrary orientation of the crystal, and temperature 10 K: (a) t_{mw}, 400 ns, 200 ns, 400 ns; both proton and nitrogen transitions are observed, arrows mark proton transitions; (b) t_{mw}, 20 ns, 100 ns, 200 ns; most of the proton transitions are suppressed due to the self-ELDOR effect; (c) suppression effect for the sequence used in a (full line shows protons; dashed line shows nitrogens); (d) suppression effect for the sequence used in b (full line shows protons; dashed line shows nitrogens).

proton and nitrogen transitions. For a mw sequence with pulse lengths 400, 200, and 400 ns, the self-ELDOR holes of the protons and nitrogens have a width of about $\Gamma_{ELDOR}/2\pi \approx 1$ MHz and are centered at $\omega_H/2\pi \approx 14$ MHz and $\omega_N/2\pi \approx 1$ MHz, respectively. Thus, only proton transitions with very small hyperfine coupling constants are reduced in intensity by the finite length of the pulses (Figure 12a). The spectrum in Figure 12b is recorded with mw pulse lengths 20, 100, and 200 ns. The short preparation pulse produces a self-ELDOR hole of width $\Gamma_{ELDOR}/2\pi \approx 25$ MHz, which strongly reduces the intensity of most of the proton ENDOR lines. The corresponding hole for the nitrogens, however, has minor influence on the intensities of the ^{14}N ENDOR transitions. In Figure 12a, the transitions which can undoubtedly be assigned to protons are marked by an arrow. The theoretical shapes of the holes (assuming $\beta_2 = \pi$ for all transitions) are shown in Figure 12, parts c and d. These plots give only a rough estimate for the ENDOR intensities; anisotropic contributions to the hyperfine couplings and nuclear

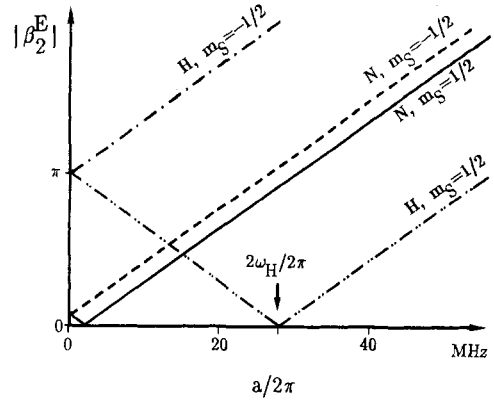

Figure 13. Effective flip angle $|\beta_2^E|$ for protons and nitrogens versus hyperfine coupling constant (proton Zeeman frequency, $\omega_H/2\pi$ = 14 MHz).

quadrupole interactions are not considered.

In the spectrum in Figure 12, proton and nitrogen lines are similar in intensities, although their gyromagnetic ratios differ by a factor of about 14. To explain this effect, we plot in Figure 13 the magnitude of the effective flip angle $|\beta_2^E| = \gamma_n|1 + (m_S a/\omega_I)|B_2 t_{rf}$ (eq 23) for protons and nitrogens as a function of the (positive) hyperfine coupling constant a. The proton Zeeman frequency is $\omega_H/2\pi$ = 14 MHz and the flip angle caused by the external field B_2 only is $\beta_{rf}(H) = -\gamma_H B_2 t_{rf} = \pi$. For proton hyperfine couplings $0 \leq a \leq 2\omega_H$ and $m_S = -1/2$, $|\beta_2^E|$ varies linearly between π and 2π, whereas for $m_S = 1/2$, $|\beta_2^E|$ drops from π to zero. In this range of the hyperfine coupling constants, transitions are induced by the left-hand rotating part of the rf field. If a becomes larger than $2\omega_H$, the transitions with $m_S = 1/2$ are induced by the right-hand rotating part of the rf field, since the effective static field at the nucleus has changed direction.

The same situation but scaled down by a factor γ_H/γ_N = 13.84 holds for nitrogen nuclei. The nuclear Zeeman frequency is reduced to $\omega_N/2\pi = (\gamma_N/\gamma_H)\omega_H/2\pi$ = 1.01 MHz and the flip angle caused by the external field B_0 to $\beta_2(N) = (\gamma_N/\gamma_H)\pi = 0.07\pi$. For nitrogen hyperfine coupling constants $a > 2\omega_N$, a condition that is usually fulfilled, the transitions in the $m_S = -1/2$ manifold are only induced by a left-hand rotating rf field, transitions in the $m_S = 1/2$ manifold only by a right-hand rotating field. This effect has been used in cw ENDOR with circularly polarized rf fields to disentangle complicated spectra.[67]

In the spectrum in Figure 12, the hyperfine coupling constants of the protons range up to 9 MHz, corresponding to an *effective* flip angle $0.7\pi < |\beta_2^E(H)| < 1.3\pi$ whereas the nitrogen hyperfine couplings lie approximately between 10 and 36 MHz, resulting in $0.3\pi < |\beta_2^E(N)| < 1.3\pi$. The similarity of the effective flip angles and, thus, of the signal intensities for protons and nitrogens is therefore a consequence of the hyperfine enhancement.

According to eq 36, which is only valid for on-resonance conditions, the ENDOR line intensity is strongly dependent on β_2. If, however off-resonance effects are included in the calculation, the peak amplitude of the ENDOR lines becomes quite insensitive to variations of β_2.[14] This is demonstrated in Figure 14a, which shows numerical simulations of the line shapes for rf flip angles $\pi/2$, π, $3\pi/2$, and 2π and a fixed rf pulse length of

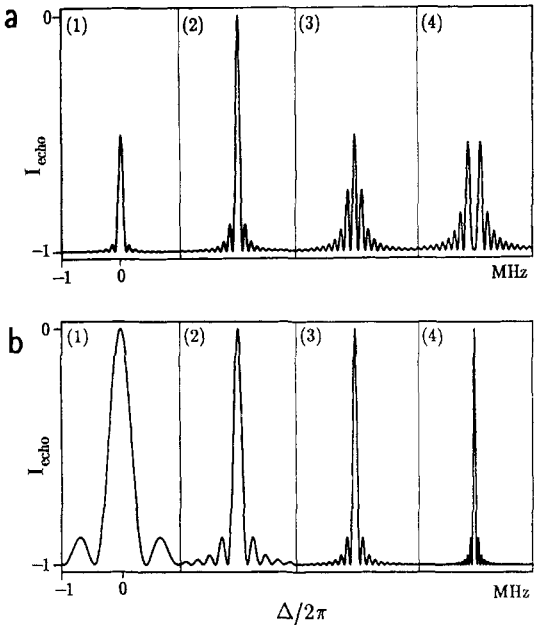

Figure 14. Simulations of ENDOR line shapes for different rf flip angles and rf pulse length, relaxation is not considered, $\Delta = \omega_{\alpha,\beta} - \omega_{rf}$: (a) pulse length, t_{rf} = 10 μs; flip angles β_2, $\pi/2$ (1), π (2), $3\pi/2$ (3), 2π (4); and (b) flip angle, $\beta_2 = \pi$; pulse lengths t_{rf}, 2 μs (1), 5 μs (2), 10 μs (3), 20 μs (4).

t_{rf} = 10 μs; relaxation effects are not considered. According to these plots, ENDOR transitions may even be observed for $\beta_2 = 2\pi$. For this particular flip angle the on-resonance signal intensity is zero, however, off-resonance effects still produce a pattern of peaks symmetric to the center frequency, which is about one half as intense compared to the on-resonance peak obtained with $\beta_2 = \pi$. This flip angle dependence has also been demonstrated experimentally.[12]

The ENDOR line shape depends also on the length of the rf pulse.[14,15] A rectangular π pulse of length t_{rf} covers a frequency range of about $2\pi/t_{rf}$ (FWHH). Since the excitation profile is convoluted with the intrinsic ENDOR line shape determined by the transverse nuclear relaxation time T_{2n}, a power broadening of the line occurs whenever t_{rf} is shorter than T_{2n}. This is true for all frequency-domain pulsed ENDOR schemes; power broadening effects are only absent in time-domain pulsed ENDOR experiments (see below). ENDOR line shapes for $\beta_2 = \pi$, $T_{2n} = \infty$ and various values of t_{rf} are plotted in Figure 14b.

Since t_{rf} is limited by the longitudinal relaxation time T_{1e} of the electron spin, one has to balance optimum signal intensity against optimum resolution. At low temperatures, where T_{1e} is sometimes of the order of milliseconds, power broadening can often be avoided. This is demonstrated in Figure 15 for nitrogen transitions between 1.7 and 4.2 MHz recorded with an rf pulse length of t_{rf} = 200 μs.[39] The line width of about 5 kHz was found to be comparable to the one observed in the corresponding cw ENDOR spectrum. Note that at these low radio frequencies the enhancement factor E is small for nitrogen and according to Figure 13 a correspondingly high rf power P is required ($B_2 \propto \sqrt{P}$) to get maximum signal intensity.

2. Mims-ENDOR

The original pulsed ENDOR scheme introduced by Mims[9] is based on the stimulated echo sequence with

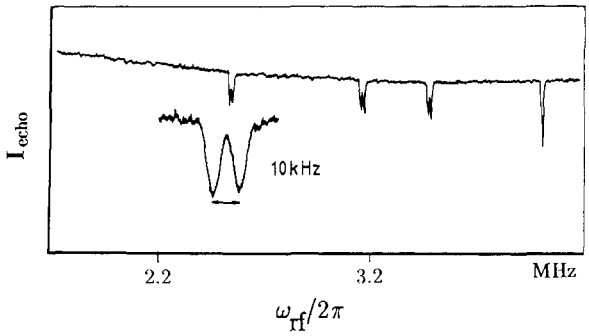

Figure 15. Single-crystal nitrogen ENDOR spectrum of bis-(*cis*-1,2-dicyanoethenedithiolate)Cu(II) in the corresponding nickel complex: τ = 500 ns; rf pulse length, t_{rf} = 200 μs; mw pulse lengths, $t_{mw}^{\pi/2}$ = 20 ns; temperature, 15 K (adapted from ref 39).

three nonselective mw $\pi/2$ pulses (Figure 5b). During the mixing period, again a selective rf pulse of variable frequency ω_{rf} and flip angle β_2 is applied. An rf pulse on-resonance with the nuclear transition $|\alpha\alpha\rangle \leftrightarrow |\alpha\beta\rangle$ changes the density operator at the end of the preparation period, σ_{prep}^{nonsel} in eq 32, to (X):

$$\sigma_{prep}^{nonsel} \xrightarrow{\beta_2 S^\alpha I_x} S_z \cos[(a/2)\tau_1] \cos(\Omega_S\tau_1) - [2S_zI_z[\tfrac{1}{2}(1 + \cos\beta_2)] + I_z[\tfrac{1}{2}(1 - \cos\beta_2)] + I_y[\tfrac{1}{2}\sin\beta_2] + 2S_zI_y[\tfrac{1}{2}\sin\beta_2]] \sin[(a/2)\tau_1] \sin(\Omega_S\tau_1) = \sigma_{mix}^{nonsel} \quad (38)$$

Note that the rf pulse has only an influence on the two spin order term $2S_zI_z$; the term with S_z is not changed during the mixing period. The nonselective mw $\pi/2$ pulse, applied after the mixing time T, creates a stimulated echo at time $T + 2\tau_1$:

$$\sigma_{mix}^{nonsel} \xrightarrow{(\pi/2)S_x} \xrightarrow{\mathcal{H}_0\tau_1} -S_y[\cos^2[(a/2)\tau_1] \cos^2(\Omega_S\tau_1) + \tfrac{1}{2}\sin^2[(a/2)\tau_1] \sin^2(\Omega_S\tau_1)(1 + \cos\beta_2)] = \sigma_{echo}^{nonsel} \quad (39)$$

Again, σ_{echo}^{nonsel} only describes the behavior of a particular spin packet. Averaging over all resonance offsets Ω_S with the spectral distribution function $g(\Omega_S) = 1$ (an assumption which is fulfilled for $\Gamma_{inh} \gg \omega_1$), results for an rf flip angle $\beta_2 = \pi$ in the echo intensity

$$I_{echo}^{nonsel} = \tfrac{1}{4}[1 + \cos(a\tau_1)] \quad (40)$$

The relative echo intensities of the Davies- and Mims-ENDOR schemes are not directly comparable, since the number of spin packets contributing to the two experiments is different.

A Mims-type powder ENDOR spectrum of a Mn(II)-doped PTC (positive temperature coefficient) ceramics[68] with nuclear transition frequencies of manganese up to 155 MHz is shown in Figure 16.[42] At these high frequencies, the enhancement factor E for the manganese nucleus amounts to 20–30, so that correspondingly weak rf field strengths are sufficient to achieve the optimum effective rf flip angle $\beta_2 = \pi$.

From eq 40 the ENDOR efficiency is determined to be

$$F_{ENDOR} = \tfrac{1}{2}\sin^2[(a/2)\tau_1] \quad (41)$$

F_{ENDOR} depends on the hyperfine coupling constant a and on τ_1, reaches its maximum for $\tau_1 = (2n + 1)\pi/a$, and is zero for $\tau_1 = 2n\pi/a$, n = 0, 1, 2, etc.[9,12] The

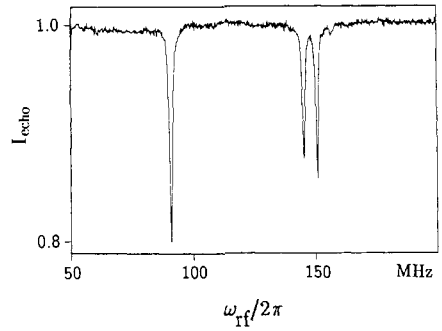

Figure 16. Mims-type Mn(II)-ENDOR spectrum of Mn(II)-doped PTC ceramics powder.[68] Parameters: t_{mw} = 20 ns; t_{rf} = 12 μs; ESR observer line, $m_I = -1/2$; temperature, 10 K (adapted from ref 42).

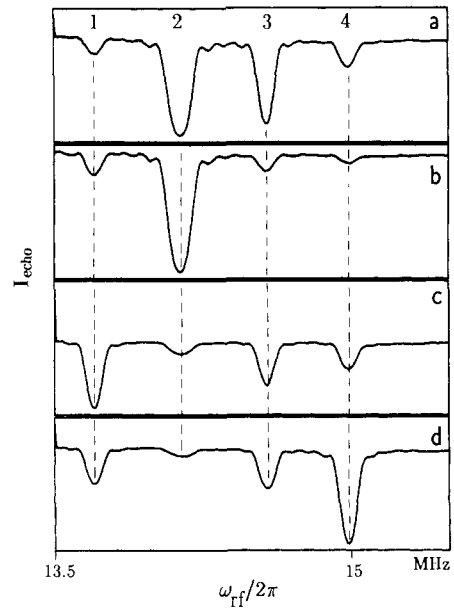

Figure 17. Intensities of four proton transitions in a Mims-ENDOR spectrum of a $Mg(NH_4)_2(SO_4)_2{\cdot}6H_2O$ single crystal doped with Cu(II) ions as a function of the pulse separation τ_1, arbitrary orientation of the crystal, and temperature 10 K: (a) τ_1 = 300 ns, (b) 340 ns, (c) 380 ns, and (d) 420 ns.

corresponding oscillatory behavior of the ENDOR line intensities as a function of τ_1, is demonstrated in Figure 17 on four proton transitions of a copper aquo complex. The amplitudes do not exactly follow eq 40. This is mainly due to the nuclear modulation effect,[23] which introduces an additional τ_1 dependence of the echo amplitude. Blind spots with zero ENDOR efficiency are observed close to τ_1 = 340 ns for transition (4) and τ_1 = 420 ns for transition (2). To avoid the possibility of missing individual lines, it is essential to repeat the experiment with different τ_1 values.

The appearance of blind spots is particularly troublesome in disordered systems, where the knowledge of the correct ENDOR line shape is often essential for the interpretation of the data. It has already been mentioned by Mims,[9] that blind spots do not occur if *selective* mw pulses are used. The theoretical description of such a Mims-ENDOR experiment is again straight forward. The average echo intensity is given by[35]

$$I_{echo}(\beta_2) = \tfrac{1}{16}(3 + \cos\beta_2) \quad (42)$$

leading to an ENDOR efficiency for $\beta_2 = \pi$ of

$$F_{ENDOR} = \tfrac{1}{4} \quad (43)$$

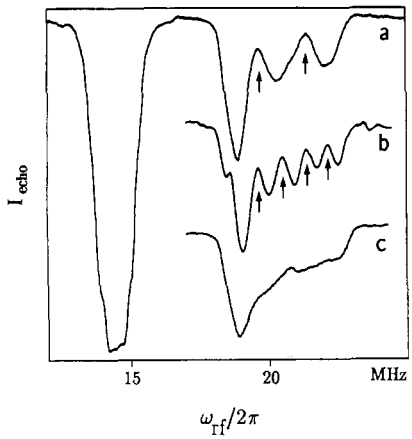

Figure 18. Part of the Mims-ENDOR spectrum of dibenzenevanadium, $V(C_6H_6)_2$, in ferrocene powder (arrows indicate blind spots), temperature 10 K: nonselective mw excitation, $t_{mw}^{\pi/2} = 10$ ns, (a) $\tau_1 = 300$ ns; (b) $\tau_1 = 600$ ns; (c) selective mw excitation, $t_{mw}^{\pi/2} = 200$ ns, $\tau_1 = 600$ ns (adapted from ref 69).

which is *independent* of the hyperfine coupling constant a.

The effect of the mw pulse length on the shape of a powder spectrum in a Mims-ENDOR experiment on dibenzenevanadium diluted in ferrocene is illustrated in Figure 18.[69] Pulses with a length of 10 ns are nonselective for both the ferrocene protons ($a/2\pi < 3$ MHz) and the benzene protons ($a/2\pi$ between 9 and 18 MHz). Since the hyperfine coupling of the benzene protons varies across the high-frequency ENDOR line, the signal intensity shows pronounced oscillations, which increase in frequency with increasing τ_1 values (Figure 18, parts a and b). However, if the lengths are increased to 200 ns, the pulses become selective with respect to the large couplings of the benzene protons and an undistorted powder line shape is obtained (Figure 18c).

C. Advanced Polarization Transfer ENDOR Techniques

In this subsection, we describe a number of new ENDOR schemes that have been developed to optimize the ENDOR effect, to determine the number of equivalent and nonequivalent nuclear spins, or to simplify complex ENDOR spectra. All these techniques are based on the transfer and subsequent detection of polarization.

1. Optimized Polarization Transfer ENDOR

In the previous section we found that in both the Davies- and the Mims-ENDOR experiment, the echo fully vanishes under optimum conditions; the ENDOR efficiency is 0.5 (50%). It is possible, however, to increase the ENDOR efficiency to 1 (100%, echo inversion) by using proper mixing processes. In principle, there exist several ways to reach this goal.

An ENDOR efficiency $F_{ENDOR} = 1$ could be obtained with a *nonselective* rf π pulse that simultaneously inverts the population of the two nuclear transitions $|\alpha\alpha\rangle \leftrightarrow |\alpha\beta\rangle$ and $|\beta\alpha\rangle \leftrightarrow |\beta\beta\rangle$ (IX):

$$2S_zI_z \xrightarrow{\beta_2 I_x} 2S_zI_z \cos\beta_2 \qquad (44)$$

As this would not allow any ENDOR resolution and is also technically impossible due to the large frequency spread, one might consider the application of two selective pulses separately to the two nuclear transitions in analogy to a "special triple" experiment:[70]

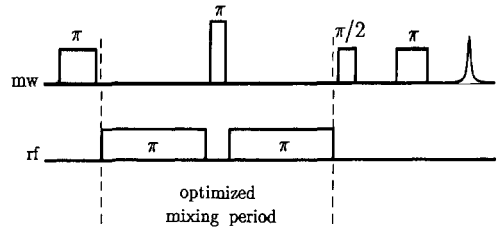

Figure 19. Davies-ENDOR pulse scheme with optimized polarization transfer to obtain an ENDOR efficiency $F_{ENDOR} = 1$. The mixing period consists of a nonselective mw π pulse sandwiched by two rf π pulses.

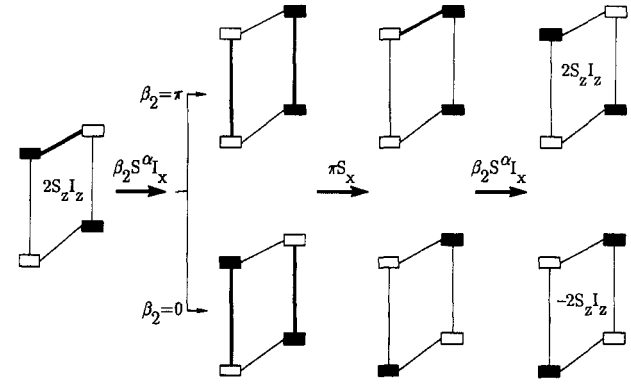

Figure 20. Effect of the optimized mixing sequence on the populations of the energy levels in a Davies-ENDOR experiment. The rf pulse is on-resonance with the nuclear transition $|\alpha\alpha\rangle \leftrightarrow |\alpha\beta\rangle$.

$$2S_zI_z \xrightarrow{\beta_2 S^{\alpha}I_x} \xrightarrow{\beta_2 S^{\beta}I_x} 2S_zI_z \cos\beta_2 \qquad (45)$$

However, if the frequency of one transition is known, the frequency of the corresponding transition in the other m_S manifold is usually unknown (see eq 2). A way out is offered by the recognition that the second selective pulse in eq 45 is equivalent to a composite pulse of the form

$$\xrightarrow{\beta_2 S^{\beta}I_x} = \xrightarrow{\pi S_x} \xrightarrow{\beta_2 S^{\alpha}I_x} \xrightarrow{\pi S_x} \qquad (46)$$

which consists of a selective rf pulse on transition $|\alpha\alpha\rangle \leftrightarrow |\alpha\beta\rangle$ sandwiched between two nonselective mw pulses. Since the second mw pulse only changes the sign of the echo signal, it can be omitted. In the Davies-ENDOR approach, the new mixing process shown in Figure 19 changes σ_{prep}^{sel} of eq 30 to

$$\sigma_{prep}^{sel} = 2S_zI_z \xrightarrow{\beta_2 S^{\alpha}I_x} \xrightarrow{\pi S_x} \xrightarrow{\beta_2 S^{\alpha}I_x} -2S_zI_z \cos\beta_2 = \sigma_{mix}^{sel} \qquad (47)$$

For $\beta_2 = 0$ and $\beta_2 = \pi$, the echo intensity is $I_{echo} = {}^1/_2$ and $-{}^1/_2$, respectively, corresponding to an ENDOR efficiency $F_{ENDOR} = 1$. The effect of this extended mixing period on the energy level populations is shown in Figure 20. It has been demonstrated that also in the Mims-ENDOR experiment carried out with nonselective or selective pulses an efficiency $F_{ENDOR} = 1$ can be achieved.[35]

The influence of the improved mixing process on a proton ENDOR transition is shown in Figure 21. It is apparent from this plot that the standard mixing period in this Davies-ENDOR experiment reduces the

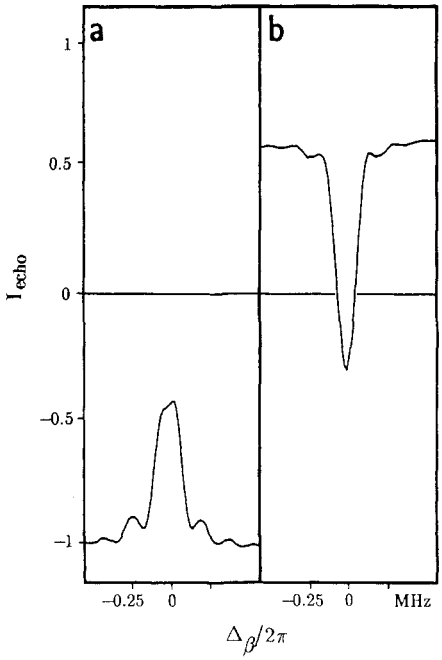

Figure 21. Effect of the optimized mixing sequence on a proton transition at $\omega_{rf}/2\pi$ = 10.15 MHz ($\Delta_\beta = \omega_\beta - \omega_{rf}$) in a Cu(II)-doped triglycine sulfate single crystal, arbitrary orientation of the crystal, and temperature 10 K, with parameters of t_{mw}^{π} = 80 ns, $t_{mw}^{\pi/2}$ = 40 ns, T = 13 μs, τ_2 = 400 ns: (a) standard mixing process (one rf pulse with $\beta_2 = \pi$ and length t_{rf} = 4.5 μs); (b) optimized mixing process (two rf π pulses of length t_{rf} = 4.5 μs and an additional mw π pulse (t_{mw}^{π} = 20 ns) between the rf pulses) (adapted from ref 35).

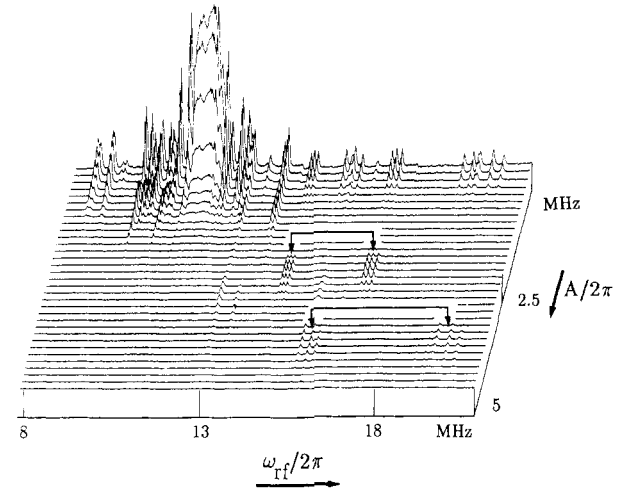

Figure 22. Two-dimensional proton-ENDOR spectrum of a $La_2Mg_3(NO_3)_{12}\cdot 24H_2O$ single crystal doped with Mn(II). The Fourier transform with respect to τ_1 adds a hyperfine dimension to the frequency dimension. Brackets connect peaks that belong to the same proton, temperature 4.2 K (adapted from ref 17).

echo intensity to about $^2/_5$ of its value without an rf pulse, resulting in an ENDOR efficiency F_{ENDOR} = 0.3, whereas the new period leads to F_{ENDOR} = 0.75. Note, however, that the additional mw π pulse reduces the intrinsic echo intensity $I_{echo}(0)$ to 0.6, since this mixing pulse is usually not strong enough to completely invert the electron spin polarization.

2. Two-Dimensional ENDOR

In section IV.B we have demonstrated that the signal intensity in a Mims-ENDOR experiment with nonselective mw pulses oscillates as a function of the time interval τ_1, resulting in the formation of blind spots for certain τ_1 values (eq 40). To eliminate this drawback, de Beer et al.[17] proposed to record the echo amplitude as a function of both the radio frequency and the time τ_1 between the first two mw $\pi/2$ pulses and to take the Fourier transformation with respect to τ_1. This results in a 2D spectrum with the radio frequency along one axis and the hyperfine coupling constant along the other axis. In such a 2D plot of the data, the assignment of the peaks belonging to the same nucleus becomes straightforward, since they all appear at the same hyperfine value. An experimental example of such a 2D-ENDOR spectrum is shown in Figure 22.

The 2D technique is restricted to hyperfine couplings that are smaller than the frequency range covered by the mw pulses. Since the echo as a function of τ_1 decays with the short phase memory time T_M, the method also suffers from poor resolution along the hyperfine axis.

3. Hyperfine-Selective ENDOR

An rf pulse applied in a Davies-ENDOR experiment to one of the nuclear transitions in the $S = {}^1/_2$, $I = {}^1/_2$ spin system changes the electron spin polarization of *both* ESR transitions by the same amount (eq 34, Figure 6). The ENDOR effect may therefore not only be observed on the ESR transition initially driven by the first mw pulse (transition $|\alpha\alpha\rangle \leftrightarrow |\beta\alpha\rangle$ in eq 35), but also on transition $|\alpha\beta\rangle \leftrightarrow |\beta\beta\rangle$ that is separated from transition $|\alpha\alpha\rangle \leftrightarrow |\beta\alpha\rangle$ by the hyperfine coupling constant a:

$$\sigma_{mix}^{sel} \xrightarrow{\pi/2S_xI^\beta} \xrightarrow{\mathcal{H}_0\tau_2} \xrightarrow{\pi S_xI^\beta} \xrightarrow{\mathcal{H}_0\tau_2} -S_yI^\beta[{}^1/_2(1 + \cos\beta_2)] = \sigma_{echo}^{sel} \quad (48)$$

The result is opposite in sign to the one obtained by observing transition $|\alpha\alpha\rangle \leftrightarrow |\beta\alpha\rangle$ (see eq 35 and Figure 6). Considering the inhomogeneity of the ESR line, the change of the observer position by the hyperfine coupling constant corresponds to recording the ENDOR effect on one of the two side holes instead on the center hole (Figure 7c), with a relative side-hole intensity:

$$I_{echo}^{sel}(\beta_2) = {}^1/_8(3 + \cos\beta_2) \quad (49)$$

For an rf pulse with flip angle $\beta_2 = \pi$, the side-hole intensity changes from $I_{echo}^{sel}(0) = {}^1/_2$ (no side hole) to $I_{echo}^{sel}(\pi) = {}^1/_4$, compared to $I_{echo}^{sel}(0) = -{}^1/_2$ and $I_{echo}^{sel}(\pi) = 0$ for the center hole.

Since the two side holes are separated from the center hole by the hyperfine coupling constant a, the position of the side holes will, in general, be different for different nuclei. In a multispin system, a transfer of magnetization and, thus, a creation of a side hole will only occur, if the radio frequency ω_{rf} corresponds to one of the ENDOR transition frequencies of a nucleus with hyperfine coupling constant a; a selection principle that is valid for any value of the nuclear spin quantum number I. The hyperfine-selective ENDOR technique,[36] therefore, enables one to select from a complex ENDOR spectrum only those lines that belong to a nucleus with a particular hyperfine coupling constant. The experiment can be repeated for a set of different hyperfine splittings, thereby decomposing the ENDOR spectrum into a number of separate spectra. Each of them describes an electron-nuclear subsystem and can be considered as a section of a two-dimensional hy-

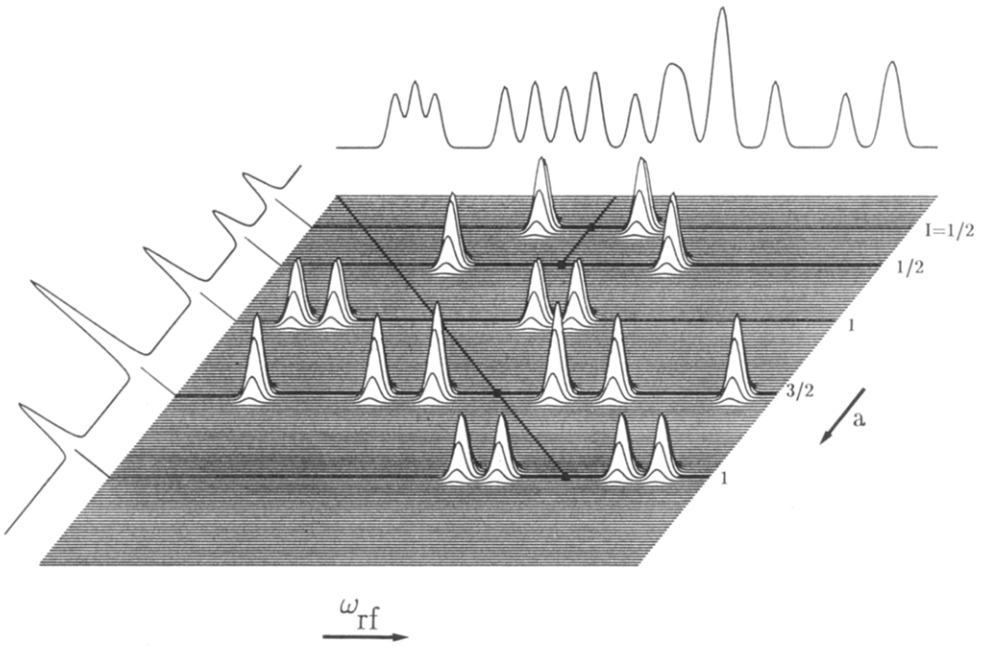

Figure 23. Schematic stack plot illustrating the disentangling of subsystem spectra (two $I = {}^1/_2$, two $I = 1$, and one $I = {}^3/_2$ nuclei) along the hyperfine dimension in hyperfine-selective ENDOR, together with the projections onto the frequency and the hyperfine axis.

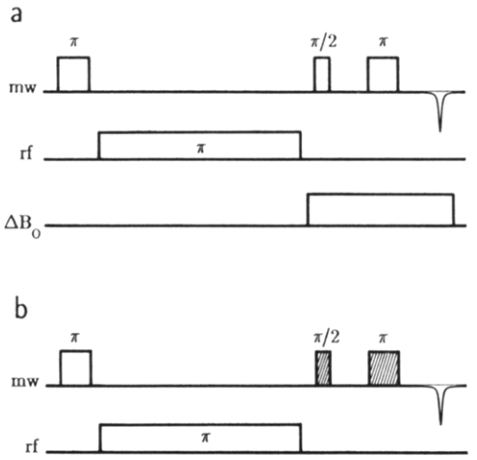

Figure 24. Pulse sequences for hyperfine-selective ENDOR: (a) pulse sequence with a field jump ΔB_0 and (b) pulse sequence with two mw frequencies.

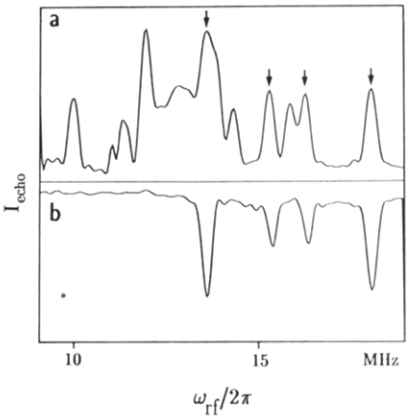

Figure 25. ENDOR spectra of Cu(II)picolinate diluted in a single crystal of the corresponding nickel complex, arbitrary orientation of the crystal, and temperature 10 K: (a) portion of the Davies-ENDOR spectrum (arrows denote positions of nitrogen transitions) and (b) field-jump hyperfine-selective ENDOR spectrum of the two magnetically equivalent ^{14}N nuclei (field jump ΔB_0 = 1.1 mT) (adapted from ref 36).

perfine-selective ENDOR display. Figure 23 shows a schematic stack plot together with the projection onto the frequency axis representing the ENDOR spectrum and the projection onto the hyperfine axis, representing the "hyperfine spectrum".

Experimentally, the change of the observer position in the ESR spectrum after the mixing period by the hyperfine coupling constant a may be achieved either by a jump of the external field, $\Delta B_0 = a\hbar/g_e\beta_e$ or by a corresponding change of the mw frequency, $\Delta\omega_{mw} = a$ (Figure 24). Since in the latter case two mw frequencies and one radio frequency are involved in the experiment, hyperfine-selective ENDOR may be considered as a kind of electron–electron–nuclear triple resonance.

We now give two experimental examples to illustrate the method. Figure 25a shows part of the ENDOR spectrum of a copper complex with proton and nitrogen lines.[36] A discrimination between the two types of nuclei is hardly possible from this spectrum. The hyperfine-selective ENDOR spectrum in Figure 25b has been recorded with a field jump ΔB_0 of 1.1 mT corresponding to a hyperfine splitting $a/2\pi$ = 31.1 MHz. The resulting spectrum consists of a four-line pattern typical for a $I = 1$ nucleus, Figure 1e (or as in the present example, of two equivalent nitrogen nuclei with unresolved second-order splitting, Figure 1f). The intensity variations are traced back to the partial resolution of the hyperfine structure in the ESR spectrum ($\Gamma_{inh} \lesssim a$).

In the second example, a frequency jump instead of a field jump is used.[37] Figure 26a shows a Davies-ENDOR spectrum of the malonic acid radical $^{\bullet}CH(COOH)_2$, recorded with the B_0 field set to the low-field line of the doublet in the ESR spectrum. The hyperfine-selective ENDOR spectrum shown in Figure 26b is observed when setting the mw detection frequency 38.6 MHz above the frequency used during the preparation period. The observed subspectrum consists of a doublet arising from the hyperfine coupling of the α

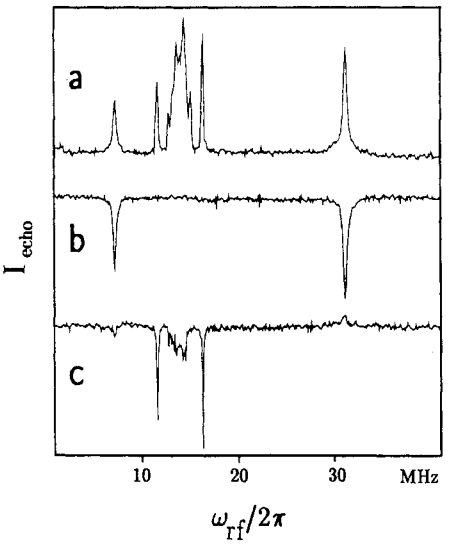

Figure 26. Single-crystal ENDOR spectra of the malonic acid radical, temperature 85 K: (a) Davies-ENDOR, (b) frequency-jump hyperfine-selective ENDOR of the α-proton (frequency jump $\Delta\omega_{mw}/2\pi$ = 38.6 MHz), and (c) frequency-jump hyperfine-selective ENDOR of one of the carboxyl protons ($\Delta\omega_{mw}/2\pi$ = 5.17 MHz) (adapted from ref 37).

proton of the CH fragment. All the more weakly coupled protons have been filtered from the spectrum. The hyperfine-selective ENDOR spectrum in Figure 26c is obtained with a frequency jump of $\Delta\omega_{mw}/2\pi$ = 5.17 MHz corresponding to the hyperfine coupling with one of the carboxyl protons. Recently, frequency-jump hyperfine-selective ENDOR has also been applied to unravel the ENDOR spectrum of a copper protein.[38]

The main advantage of hyperfine-selective ENDOR is its capability to measure an ENDOR subspectrum of a single crystal or a powder originating exclusively from nuclei with a preselected hyperfine coupling constant. Thereby, the hyperfine selectivity is determined by the width of the side holes that decreases with increasing mw pulse lengths. The resolution along the hyperfine axis in a hyperfine-selective ENDOR experiment is therefore superior to the one in 2D-ENDOR, provided the signal-to-noise ratio allows one to use sufficiently long mw pulses.

4. Triple Resonance

In a triple resonance (or double ENDOR) experiment, nuclear transitions are excited with two rf fields of different frequency. Initially, cw triple resonance was introduced to determine relative signs of hyperfine coupling constants in single crystals.[71] Later, the technique has also been used to separate overlapping ENDOR spectra,[4,72] to improve the orientation selectivity in disordered systems,[73] and to enhance the resolution in liquids.[70,74]

In the pulsed version of triple resonance, the mixing period consists of two rf π pulses separated in time by ΔT (Figure 27).[45,75] The first rf pulse with fixed frequency ω_{rf2} is on-resonance with a nuclear transition, while the second rf field with frequency ω_{rf1} is swept through the ENDOR spectrum. The population inversion of a particular nuclear transition caused by rf2 in one of the two m_S manifolds changes the echo signal intensities of all nuclear transitions that have a level in common with the ESR transition excited by the mw preparation pulse.

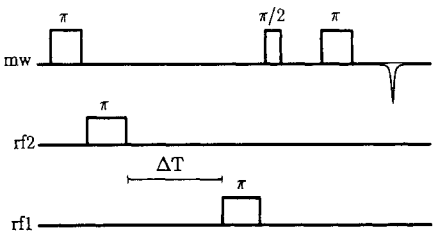

Figure 27. Pulse scheme for electron–nuclear–nuclear triple resonance. The radio frequency rf2 is on-resonance with one of the nuclear transitions. Radio frequency rf1 is swept.

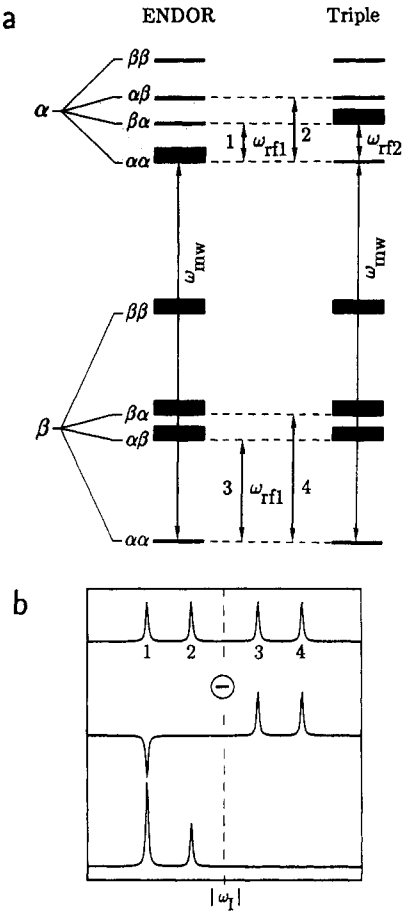

Figure 28. Energy level diagram for a $S = {}^1/_2$, $I_1 = {}^1/_2$, $I_2 = {}^1/_2$ spin system with hyperfine couplings $a_1, a_2 > 0$, $|a_1/2|, |a_2/2| < |\omega_I|$, and corresponding ENDOR and triple resonance spectra: (a) (left) ENDOR experiment (populations after the selective mw pulse on-resonance with transition $|\alpha\alpha\alpha\rangle \leftrightarrow |\beta\alpha\alpha\rangle$); (right) triple resonance experiment (populations after the first rf pulse on-resonance with nuclear transition $|\alpha\alpha\alpha\rangle \leftrightarrow |\alpha\beta\alpha\rangle$); (b) (top) ENDOR spectrum, (middle) triple resonance spectrum, and (bottom) difference triple spectrum.

The description of the triple resonance experiment with the product operator formalism is again straightforward. However, since the spin dynamics in this approach is basically the same as the one in a Davies-ENDOR experiment, we discuss the technique only with the help of the energy level diagram for a three-spin system $S = {}^1/_2$, $I_1 = {}^1/_2$, $I_2 = {}^1/_2$ with hyperfine couplings $a_1 > a_2 > 0$ and $|a_1/2|, |a_2/2| < |\omega_I|$.

The selective mw preparation pulse inverts the electron spin polarization of transition $|\alpha\alpha\alpha\rangle \leftrightarrow |\beta\alpha\alpha\rangle$ (Figure 28a, left), resulting in an echo intensity $I_{echo} = -{}^1/_2$ at the end of the detection sequence. The ENDOR spectrum shown in Figure 28b (top) is obtained by sweeping ω_{rf1} through the ENDOR spectral range and

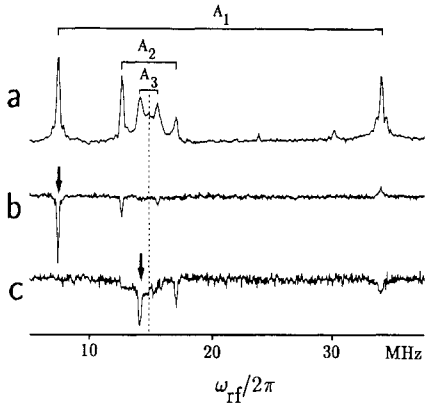

Figure 29. Single-crystal ENDOR and difference triple spectra of the malonic acid radical at room temperature: (a) Davies-ENDOR spectrum; (b) difference triple spectrum, fixed radio frequency $\omega_{rf2}/2\pi$ on-resonance with the transition at 7.5 MHz (indicated by an arrow), $\Delta T = 0$; and (c) difference triple spectrum, fixed radio frequency $\omega_{rf2}/2\pi$ on-resonance with the transition at 14 MHz (indicated by an arrow), $\Delta T = 0$ (adapted from ref 75).

consists of two transitions at frequencies $|a_1/2 + \omega_I|$ (1) and $|a_2/2 + \omega_I|$ (2) in the $m_S = {}^1/_2$ manifold, and two transitions at frequencies $|a_2/2 - \omega_I|$ (3) and $|a_1/2 - \omega_I|$ (4) in the $m_S = -{}^1/_2$ manifold. In the triple resonance experiment, on the other hand, the first rf pulse with frequency ω_{rf2} inverts the nuclear spin polarization between the levels $|\alpha\alpha\alpha\rangle$ and $|\alpha\beta\alpha\rangle$ thereby eliminating the polarization of the ESR transition selectively excited by the mw pulse (Figure 28a, right).

A sweep through the ENDOR spectral range of the rf field with frequency ω_{rf1} results in the triple resonance spectrum shown in Figure 28b (middle). The changes in line intensity obtained in the two experiments are best demonstrated by subtracting the triple resonance spectrum from the ENDOR spectrum. The resulting "difference triple spectrum" (Figure 28b, bottom) reflects only those transitions for which one energy level is a common level of the ESR transition and the transition excited by ω_{rf2}, (level $|\alpha\alpha\alpha\rangle$ in Figure 28a). Thus, all transitions observed in a difference triple spectrum belong to the *same* m_S manifold. This result can be used to determine the relative sign of hyperfine coupling constants. If a transition lies on the same side with respect to the nuclear Zeeman frequency $|\omega_I|$ as the one excited by ω_{rf2}, the sign of the two coupling constants is the same; if the two transitions lie on opposite sides, the coupling constants are different in sign.

The behavior of difference triple spectra is again exemplified on the malonic acid radical.[75] In the Davies-ENDOR spectrum in Figure 29a, the six prominent lines can be assigned to three protons with hyperfine coupling constants A_1, A_2, and A_3. The difference triple spectrum in Figure 29b has been recorded with a fixed radiofrequency $\omega_{rf2}/2\pi = 7.5$ MHz. Three negative going peaks are obsereved, namely the reference peak at 7.5 MHz, the low-frequency peak of A_2, and the high-frequency peak of A_3. Since A_1 is negative for theoretical reasons,[76] all observed peaks belong to the $m_S = -{}^1/_2$ manifold. It then immediately follows from the triple spectrum that A_2 is also negative and A_3 is positive. The incomplete suppression of the high-frequency peak at 34 MHz is traced back to relaxation effects.[75] Figure 29c shows the corresponding transitions in the $m_S = {}^1/_2$ manifold obtained with ω_{rf2}

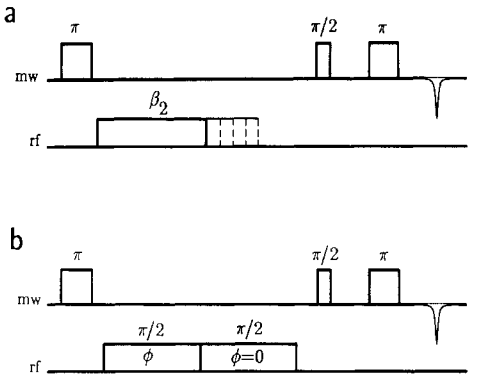

Figure 30. Pulse sequences for the measurement of nuclear transient nutations and multiple quantum coherences: (a) incrementation of the rf pulse length and (b) incrementation of the phase angle ϕ of the first rf $\pi/2$ pulse.

set at the low-frequency peak of the proton with hyperfine coupling constant A_3. Recently, pulsed triple resonance has been used to determine the relative signs of hyperfine couplings constants in isotropic *trans*-polyacetylene.[32]

By varying the time ΔT between the two rf pulses, triple resonance may also be applied to determine complex relaxation pathways and to investigate cross-relaxation connectivities.[75]

5. ESR-Detected Nuclear Transient Nutations and Multiple Quantum ENDOR

In a polarization transfer ENDOR experiment, the magnetization of the excited nuclear transition nutates in the plane perpendicular to the applied rf field vector. In the two standard pulsed ENDOR schemes described in section IV.B, this nutation is terminated for a flip angle $\beta_2 = \pi$. If the rf pulse remains on, the magnetization continues to rotate, thereby periodically exchanging energy between the spin system and the rf field. This nuclear transient nutation phenomenon becomes immediately evident in our operator formalism if, for example, the expression for σ_{mix}^{sel} in eq 34 is rearranged to give

$$\sigma_{mix}^{sel} = S^\alpha I_z \cos\beta_2 - S^\alpha I_y \sin\beta_2 - S^\beta I_z \qquad (50)$$

A corresponding expression for the Mims-ENDOR approach may be derived from eq 38. According to eq 50, both polarization and coherence of the driven nuclear transition $|\alpha\alpha\rangle \leftrightarrow |\alpha\beta\rangle$ oscillate with frequency ω_2. The polarization of the other nuclear transition, $|\beta\alpha\rangle \leftrightarrow |\beta\beta\rangle$, remains unchanged during the mixing period.

In the following, we discuss two methods for generating and detecting such nutation effects and demonstrate that both schemes are equivalent. The first approach involves a stepwise increase in the rf pulse length (Figure 30a),[34] whereas in the second scheme two rf pulses with the same flip angle are used and the phase of one of the pulse is advanced in a stepwise fashion (Figure 30b).[33] To prove the equivalency of these two approaches, we first consider a selective rf pulse with arbitrary phase ϕ defined as the displacement from the x axis toward the y axis:

$$\beta_2 S^\alpha I_\phi = \beta_2(S^\alpha I_x \cos\phi + S^\alpha I_y \sin\phi) \qquad (51)$$

This corresponds to a rotation with angle $-\phi$ around the z axis followed by a β_2 rotation around x and a ϕ rotation around z.[77] The selective rf pulse in eq 51 can

therefore be expressed as a series of three rotations (XII):

$$\xrightarrow{\beta_2 S^\alpha I_\phi} = \xrightarrow{-\phi S^\alpha I_z} \xrightarrow{\beta_2 S^\alpha I_x} \xrightarrow{\phi S^\alpha I_z} \quad (52)$$

The two-spin order term $2S_zI_z$ created by the mw preparation pulse is then transformed by such an rf pulse into

$$\sigma^{sel}_{prep} = 2S_zI_z = S^\alpha I_z - S^\beta I_z \xrightarrow{\beta_2 S^\alpha I_\phi} S^\alpha I_z \cos\beta_2 - S^\beta I_z + S^\alpha I_x \sin\phi \sin\beta_2 - S^\alpha I_y \cos\phi \sin\beta_2 \quad (53)$$

In the experiment in Figure 30a, where the rf pulse length is incremented, eq 53 describes the state of the density operator at the end of the mixing period. From the first two terms, the polarization of the observed ESR transition $|\alpha\alpha\rangle \leftrightarrow |\beta\alpha\rangle$ is calculated to be

$$\sigma^{sel}_{mix} = S_zI^\alpha[\tfrac{1}{2}(1 + \cos\beta_2)] \quad (54)$$

a result that is independent on ϕ and is also contained in eq 34.

In the phase incrementation experiment (Figure 30b) on the other hand, the second rf pulse with fixed phase $\phi = 0$ transfers the nuclear coherence along y created by the first half of the mixing period (last term in eq 53) to observable polarization

$$-S^\alpha I_y \cos\phi \sin\beta_2 \xrightarrow{\beta_2 S^\alpha I_x} S^\alpha I_z[\cos^2(\beta_2) - \sin^2(\beta_2)\cos\phi] - S^\beta I_z = \sigma^{sel}_{mix} \quad (55)$$

If again only the polarization of transition $|\alpha\alpha\rangle \leftrightarrow |\beta\alpha\rangle$ is considered, eq 55 reduces to

$$\sigma^{sel}_{mix} = S_zI^\alpha[\tfrac{1}{2}[1 + \cos^2(\beta_2) - \sin^2(\beta_2)\cos\phi]] \quad (56)$$

It is evident from eq 54 and 56, that both experiments become equivalent, if in the first scheme the flip angle β_2 is varied $[^1/_2(1 + \cos\beta_2)]$ and in the second scheme, with $\beta_2 = \pi/2$, the phase ϕ is incremented $[^1/_2(1 - \cos\phi)]$. The phase difference of 180° between the oscillations in the two approaches is due to the fact that the mixing period of the second scheme starts with a total flip angle $2\beta_2 = \pi$. It is interesting to note that in the latter experiment, β_2 has no influence on the oscillation frequency; a deviation of β_2 from the optimum value $\beta_2 = \pi/2$ simply reduces the amplitude of the oscillation.

In the two approaches described above, either the flip angle β_2 or the phase angle ϕ has to be incremented step by step, each providing one data point. However, it is also possible to measure the entire nuclear transient nutation pattern in a single experiment.[34,78] Two such schemes are shown in Figure 31. In the sequence in Figure 31a, electron spin polarization is again transferred to the nuclear spins by a selective mw π pulse. The nuclear transient nutation during rf irradiation of constant amplitude and fixed total length T is now *continuously* monitored by a weak mw probe field that has no saturating effect on the electron spin polarization. With this extended-time detection, the entire nutation pattern is obtained in a *single* experiment. The photograph in Figure 32a shows such a nuclear transient nutation of a copper-ENDOR transition at 18.8 MHz, recorded with an rf field strength of $B_2 = 0.9$ mT.

The nuclear transient nutation experiment can even be realized with continuous microwave excitation (Figure 31b). The mw irradiation is now used to create

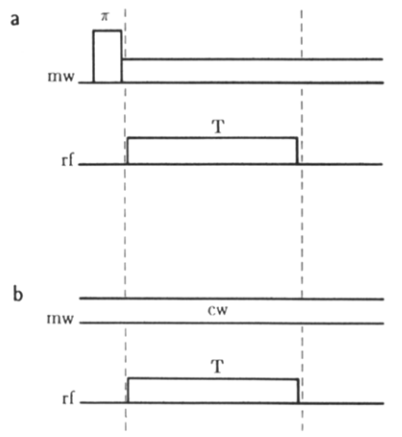

Figure 31. Pulse schemes for extended-time detection of nuclear transient nutations: (a) preparation and detection mw pulses are separated in time and (b) weak mw irradiation is used for both creation and indirect detection of nuclear spin polarization.

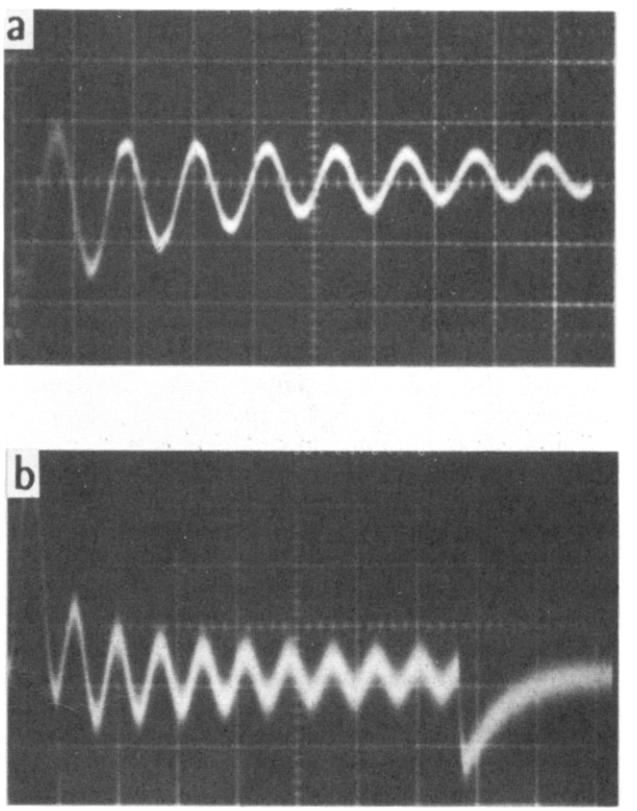

Figure 32. Nuclear transient nutation patterns of a copper-ENDOR transition in a Cu(II)-doped $Mg(NH_4)_2(SO_4)_2{\cdot}6H_2O$ single crystal; $\omega_{rf}/2\pi = 18.8$ MHz; time axis, 2 μs per div; temperature 10 K: (a) detected with scheme a of Figure 31 ($B_2 = 0.9$ mT); and (b) detected with scheme b of Figure 31 (adapted from ref 34).

nuclear polarization during the time before the rf pulse is turned on ($t < 0$), as well as indirectly to detect the oscillating nuclear polarization during application of the rf pulse ($t > 0$). Obviously, this experiment is not optimum, since for $t < 0$ the mw field should be sufficiently strong to saturate an ESR transition, whereas for $0 < t < T$, the irradiation should be weak enough such that the electron spin polarization is not modified by the mw probe field. A nuclear transient nutation observed with this pulse sequence is shown in Figure 32b.

Apart from the determination of the rf field strength,[34,75] the observation of nuclear transient nu-

tations in a spin system with one nucleus is not of much practical use. However, this situation changes, if more than one nucleus is considered. We demonstrate this for a spin system with two equivalent nuclei with spin $I = {}^1/_2$, described by the rotating frame Hamiltonian given in eq 15 ($a_1 = a_2$). Application of a selective mw π pulse to the equilibrium state generates terms of the form

$$-S_z \xrightarrow{\pi S_x I_{1x} I_{2x}} S_z,\ 2S_zI_{1z},\ 2S_zI_{2z},\ 4S_zI_{1z}I_{2z} \qquad (57)$$

The first three terms have already been described before. The term $4S_zI_{1z}I_{2z}$ on which we will concentrate in the following, represents longitudinal three-spin order. A selective rf pulse of phase ϕ applied in the $m_S = {}^1/_2$ manifold of the electron spin generates terms of the form[58]

$$4S_zI_{1z}I_{2z} = 2S^\alpha I_{1z}I_{2z} - 2S^\beta I_{1z}I_{2z} \xrightarrow{\beta_2(S^\alpha I_{1\phi} + S^\alpha I_{2\phi})} 2S^\alpha I_{1z}I_{2z}\cos^2(\beta_2),\ 2S^\alpha I_{1y}I_{2y}\sin^2(\beta_2)\cos^2\phi \qquad (58)$$

In eq 58 only the electron–nuclear three-spin order and the term describing nuclear two-spin coherence, in antiphase with respect to the electron spin, are considered. In the experiment with variable β_2 and $\phi = 0$ (Figure 30a), the three-spin order term

$$2S^\alpha I_{1z}I_{2z}[{}^1/_2[1 + \cos(2\beta_2)]] = \sigma^{sel}_{mix} \qquad (59)$$

introduces an additional oscillation with frequency $2\omega_2$ ($2\beta_2 = 2\omega_2 t_{rf}$).

In the experiment with variable phase ϕ and $\beta_2 = \pi/2$ (Figure 30b), the second rf pulse with $\phi = 0$ transfers the nuclear two-spin coherence in eq 58 back to three-spin order:

$$2S^\alpha I_{1y}I_{2y}\cos^2\phi \xrightarrow{(\pi/2)(S^\alpha I_{1x} + S^\alpha I_{2x})} 2S^\alpha I_{1z}I_{2z}[{}^1/_2[1 + \cos(2\phi)]] = \sigma^{sel}_{mix} \qquad (60)$$

From eqs 59 and 60 it becomes again evident that the two approaches are equivalent.

The experiment with the variable phase angle ϕ is called *multiple quantum* ENDOR,[33] since nuclear multiple quantum coherence is created and transferred during the mixing period. The term $2I_{1y}I_{2y}$, for example, represents both zero quantum and double quantum coherence. Multiple quantum coherence is of course also created in the experiment with a variable rf flip angle. In this experiment the multiple quantum transitions are separated out via multiple spin orders, whereas in phase incrementation spectroscopy the different multiple quantum coherences are separated out by utilizing their rotational symmetry about the z axis. This principle is closely related to well known techniques used in multiple quantum NMR.[59]

In an ENDOR spectrum (cw or pulsed) the number of equivalent nuclei contributing to an ENDOR transition is not reflected in the intensity of this transition, i.e. information about multiplicities in an electron–nuclear spin system is lost. The data observed in the two multiple quantum techniques discussed in this subsection, however, contain this information. For systems with n equivalent nuclei the Fourier coefficients of the nutation or phase incrementation patterns represent a multiple quantum ENDOR spectrum with frequencies up to the nth harmonic.

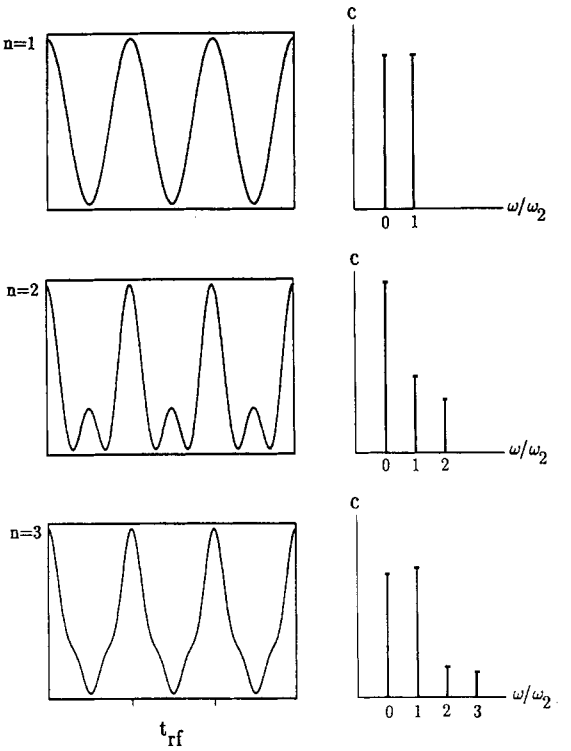

Figure 33. Computed nuclear transient nutation patterns for $n = 1$, 2, and 3 equivalent $I = {}^1/_2$ nuclei together with the corresponding Fourier coefficients c (adapted from ref 34).

In a calculation of multiple quantum peak intensities one has to keep in mind that in systems with a large inhomogeneous broadening, the selective mw preparation pulse excites all ESR transitions, but each one in a different spin packet. The observed nutation or phase incrementation trace is then the result of superimposing n multiple quantum patterns.[34] For two equivalent $I = {}^1/_2$ nuclei, for example, the echo intensity is given by

$$I_{echo} = {}^1/_{16}[9 + 4\cos(\beta_2) + 3\cos(2\beta_2)] \qquad (61)$$

For spin systems with n equivalent nuclei the highest modulation frequency is again $n\omega_2$, however, the intensities of the higher harmonics decrease rapidly with an increasing number of equivalent nuclei. Nutation patterns and the corresponding Fourier coefficients c for $n \leq 3$ are given in Figure 33.

An experimental verification for $n = 1$ and $n = 2$ is shown in Figure 34, comparing the nutation traces obtained with a vanadyl and a copper aquo complex. In the vanadyl case, the 10 water protons are not equivalent,[79] and only a single quantum transition resulting in a sinusoidal oscillation at the fundamental frequency ω_2 is observed for each ENDOR line (Figure 34a). In the corresponding copper aquo complex the 12 water protons are magnetically equivalent in pairs.[80] All ENDOR lines of these water protons therefore exhibit a modulation consisting of the fundamental frequency ω_2 and the first harmonic $2\omega_2$ as is shown in Figure 34b.

Multiple quantum ENDOR spectroscopy has also been used to determine the hyperfine spectral density in different sections of an ENDOR spectrum.[33] In this approach, the number of multiple quantum transitions that may be excited by the rf pulse within a range of $\pm\omega_2$ around the radio frequency ω_{rf} is used as a measure for the hyperfine spectral density. An illustrative example on solitons in polyacetylene with ω_{rf} close to the

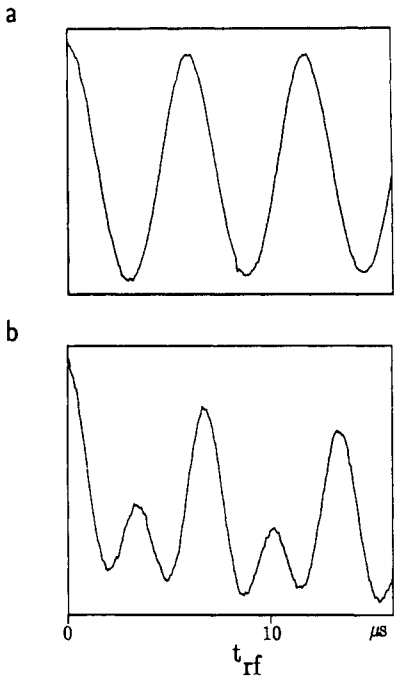

Figure 34. Experimental nuclear transient nutation pattern of protons in VO(IV)- and Cu(II)-doped $Mg(NH_4)_2(SO_4)_2{\cdot}6H_2O$ single crystals, arbitrary orientation of the crystals, temperature 10 K: (a) one proton in $VO(H_2O)_5^{2+}$, $\omega_{rf}/2\pi$ = 19.2 MHz, and (b) two magnetically equivalent protons in $Cu(H_2O)_6^{2+}$, $\omega_{rf}/2\pi$ = 15.9 MHz (adapted from ref 34).

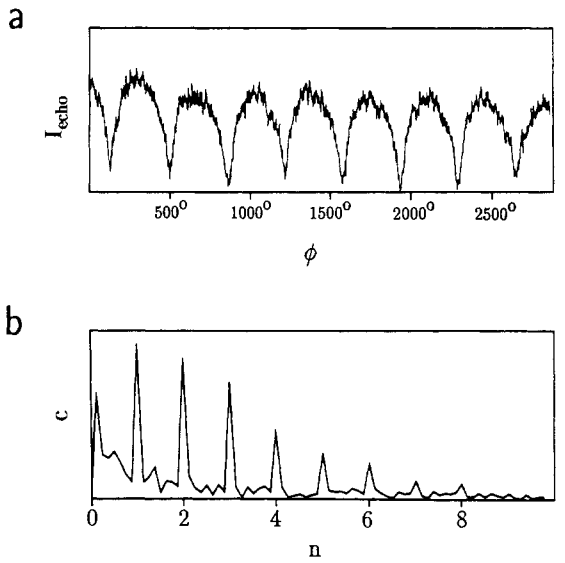

Figure 35. Multiple-quantum ENDOR response of the polyacetylene radical: (a) echo signal intensity as a function of the phase angle ϕ and (b) Fourier transformation of a (adapted from ref 47).

nuclear Zeeman frequency of the protons and $\omega_2/2\pi$ = 250 kHz in shown in Figure 35. The echo intensity is recorded as a function of the phase angle ϕ with phase increments of $\Delta\phi$ = 1.4° (Figure 35a). Fourier transformation of this trace results in a multiple quantum ENDOR spectrum (Figure 35b) containing multiple quantum frequencies up to $8\omega_2$.

In principle, with both approaches presented in this subsection, the same information is obtained. The nutation method with the incrementation of the pulse length is experimentally easier to perform than the phase incrementation. However, the former method requires a sufficiently long electron spin–lattice relaxation time to collect the data of several oscillation periods. For radicals in solution usually impeded by short relaxation times, the second technique might therefore be superior, since the mixing period is short and fixed in time during the experiment. With the high rf fields attainable today,[42,44] also in the liquid state, the observation of nuclear transient nutations should become feasible.

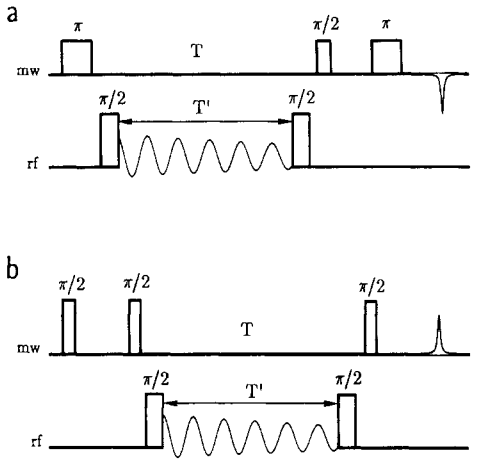

Figure 36. Pulse schemes for time-domain ENDOR: (a) scheme with selective mw pulses (Davies-type mw pulse sequence) and (b) scheme with nonselective mw pulses (Mims-type mw pulse sequence).

6. Time-Domain ENDOR

The pulsed ENDOR schemes discussed so far were basically frequency-domain techniques where the frequency ω_{rf} of the rf pulse is varied step by step. We have demonstrated in section IV.B (Figure 14b) that all these techniques suffer from a severe power broadening, if the rf pulse length is shorter than the inverse width of the ENDOR line.

Recently, Höfer et al.[27] introduced a time-domain pulsed ENDOR method in which this drawback is circumvented. The technique belongs again to the category of polarization transfer ENDOR schemes and can be performed with selective[27] as well as with nonselective mw pulses[43] (Figure 36). In both schemes, the mixing period consists of two rf $\pi/2$ pulses separated by a variable time interval T'.

In the following, we describe the experiment with selective mw pulses in more detail. After the application of a mw π pulse acting on ESR transition $|\alpha\alpha\rangle \leftrightarrow |\beta\alpha\rangle$, the density operator is again described by the two-spin order term $2S_zI_z$ (eq 30). The first nonselective rf $\pi/2$ pulse with phase angle ϕ = 0 creates the nuclear coherence (IX)

$$2S_zI_z \xrightarrow{(\pi/2)I_x} -2S_zI_y \tag{62}$$

that evolves during the free evolution time t under the rotating frame Hamiltonian $\mathcal{H}_0$ (eq 14):

$$\begin{aligned} -2S_zI_y \xrightarrow{\mathcal{H}_0 t} & -2S_zI_y \cos(\Omega_I t) \cos[(a/2)t] + \\ & 2S_zI_x \sin(\Omega_I t) \cos[(a/2)t] + \\ & I_y \sin(\Omega_I t) \sin[(a/2)t] + I_x \cos(\Omega_I t) \sin[(a/2)t] \end{aligned} \tag{63}$$

Equation 63 describes the free induction decay (FID) of the nuclear spin with the two frequencies $\Delta_\alpha = |(a/2) + \Omega_I| = \omega_\alpha - \omega_{rf}$ and $\Delta_\beta = |(a/2) - \Omega_I| = \omega_\beta - \omega_{rf}$ (see

below). The first two terms represent antiphase nuclear spin coherence that is not directly observable. The last two terms describing nuclear spin coherence along the y and x axis could, in principle, be observed with NMR induction coils along y and x, respectively. The damping of this FID is directly only affected by the transverse nuclear relaxation time.

After an evolution time T', a second nonselective rf $\pi/2$ pulse transfers the coherence back to polarization. Thus, in this time-domain ENDOR experiment, nuclear coherence is created at the beginning of the mixing period and transferred to polarization at the end of the period; a transfer of coherence, however, is not involved. For an rf pulse again along the x axis, only the first and third term in eq 63 have to be considered (VIII):

$$-2S_zI_y \cos(\Omega_I T') \cos[(a/2)T'] + I_y \sin(\Omega_I T') \sin[(a/2)T'] \xrightarrow{(\pi/2)I_x} -(S_zI^\alpha - S_zI^\beta)[\tfrac{1}{2}[\cos(\Delta_\alpha T') + \cos(\Delta_\beta T')]] - I_z[\tfrac{1}{2}[\cos(\Delta_\alpha T') - \cos(\Delta_\beta T')]] = \sigma_{mix}^{sel} \quad (64)$$

The detection sequence with mw pulses again selectively acting on transition $|\alpha\alpha\rangle \leftrightarrow |\beta\alpha\rangle$ creates from the S_zI^α term a two-pulse echo at time $T + 2\tau_2$ (eq 35):

$$\sigma_{echo}^{sel} = -S_yI^\alpha[\tfrac{1}{2}[\cos(\Delta_\alpha T') + \cos(\Delta_\beta T')]] \quad (65)$$

with the relative echo intensity

$$I_{echo}^{sel} = \tfrac{1}{2}[\cos(\Delta_\alpha T') + \cos(\Delta_\beta T')] \quad (66)$$

along the $-y$ axis. If time T' is incremented in steps, the echo intensity fully reflects the FID (real part) of the nuclear spins. In order to differentiate positive and negative frequencies with respect to ω_{rf}, quadrature readout has to be used; i.e. the experiment is repeated with the second rf pulse along the y axis, resulting in a relative echo intensity (imaginary part of the FID):

$$I_{echo}^{sel} = \tfrac{1}{2}[\sin(\Delta_\alpha T') - \sin(\Delta_\beta T')] \quad (67)$$

The ENDOR spectrum with positive and negative frequencies with respect to ω_{rf} is then obtained from a complex Fourier transformation of these data.

In a time-domain ENDOR experiment with more than one nuclear spin, also multiple quantum coherence is created and detected. In a spin system with two $I = {}^1/_2$ nuclei the first rf pulse creates the nuclear two-spin coherence $4S_zI_{1y}I_{2y}$ (eq 58). This two-spin coherence is manifested in the ENDOR spectrum by the two frequencies $\Delta_\alpha^{(2)} = (\omega_{\alpha 1} + \omega_{\alpha 2}) - 2\omega_{rf}$ and $\Delta_\beta^{(2)} = (\omega_{\beta 1} + \omega_{\beta 2}) - 2\omega_{rf}$.

Experimentally, the rf pulse can cover a spectral width of up to about $\omega_2/2\pi = 1$ MHz.[27,42,44] With such an rf pulse strength, only those transitions can be observed in the spectrum for which Δ_α and Δ_β are smaller than the excitation range. In our spin system with one $I = {}^1/_2$ nucleus, the FID contains at best one oscillation frequency, except for hyperfine couplings $a < \omega_2$, where both frequencies can be excited by using a proper setting of ω_{rf}. It is interesting to note that the excitation range of the rf pulse also depends on the hyperfine enhancement and, thus, is different for each ENDOR line.

To map out the full ENDOR spectrum, ω_{rf} has to be shifted in segments across the total spectral width. Experimental results obtained on the malonic acid radical recorded with rf increments of $\Delta\omega_{rf}/2\pi = 1$ MHz

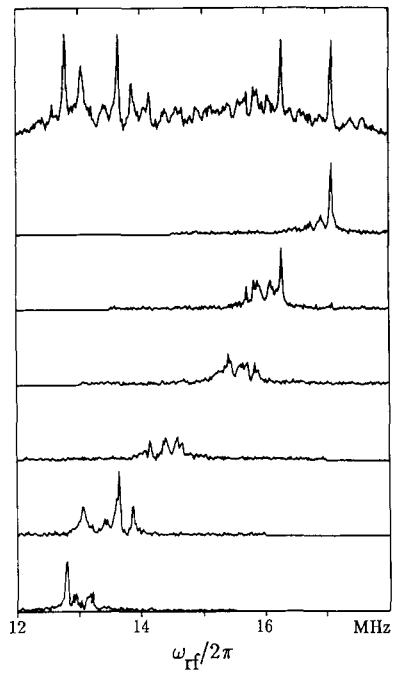

Figure 37. Time-domain ENDOR. Synthesis of the single-crystal spectrum of the malonic acid radical was by a complex Fourier transform. The spectral segments for different ω_{rf} settings are obtained by means of quadrature readout. The ENDOR spectrum (top) is the sum of the spectral segments, measured at room temperature (adapted from ref 27).

are shown in Figure 37.[27] The line shapes in this experiment are free of power broadening and correspond to the natural line shapes. Weak hyperfine interactions are not observed in such a time-domain ENDOR spectrum (Figure 37, top). This is again a consequence of the self-ELDOR effect.

Very recently it has been demonstrated that time-domain ENDOR experiments can also be performed with nonselective mw pulses (Figure 36b).[43] To describe the signals expected in this experiment, a detailed theoretical approach that also includes nonsecular electron–nuclear spin interactions has been developed.

In time-domain ENDOR the FID of the nuclear spins created by the first rf $\pi/2$ pulse may be refocused by an rf π-pulse applied at a time $T'/2$. The resulting *nuclear* spin echo formed at time T' is then converted to electron spin polarization by a second rf $\pi/2$ pulse.[27] Such an indirect detection of a nuclear spin echo allows one to study relaxation processes of individual transitions in the ENDOR spectrum.

V. Coherence Transfer ENDOR

The pulsed ENDOR methods discussed in this section are based on the transfer of coherences rather than on polarizations.[10,28] We first consider the transfer of electron spin coherence by a selective rf pulse applied to a transition that has an energy level in common with the ESR transition involved in the coherence. In our $S = {}^1/_2$, $I = {}^1/_2$ spin system the (single quantum) electron spin coherence is assumed to be of the form S_yI^α (transition $|\alpha\alpha\rangle \leftrightarrow |\beta\alpha\rangle$). The selective rf pulse with flip angle β_2 on-resonance with transition $|\alpha\alpha\rangle \leftrightarrow |\alpha\beta\rangle$ transforms this coherence to

$$S_yI^\alpha \xrightarrow{\beta_2 S^\alpha I_x} S_yI^\alpha \cos(\beta_2/2) - [\tfrac{1}{2}(2S_xI_x + 2S_yI_y) \sin(\beta_2/2)] \quad (68)$$

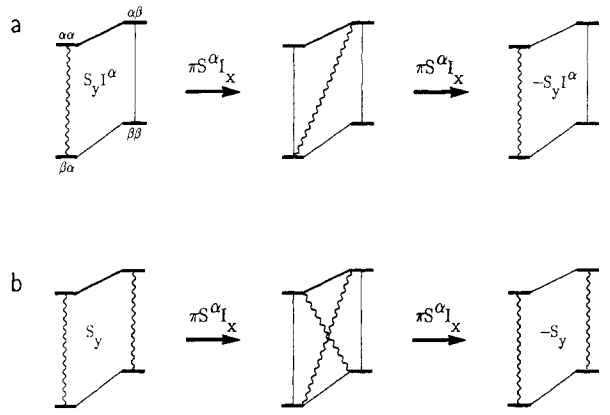

Figure 38. Transfer of electron spin coherence by a selective and a nonselective rf pulse of flip angle $\beta_2 = \pi$ and 2π, selective rf pulse on-resonance with nuclear transition $|\alpha\alpha\rangle \leftrightarrow |\alpha\beta\rangle$: (a) selective mw pulse on-resonance with ESR transition $|\alpha\alpha\rangle \leftrightarrow |\beta\alpha\rangle$ and (b) nonselective mw pulse.

It is essential to note that in eq 68 the flip angle β_2 appears to be halved after the transfer.[59] In the explicit computation of this expression, we made use of the transcriptions (XIII, XIV):

$$\xrightarrow{\beta_2 S^\alpha I_x} = \xrightarrow{(\beta_2/2)I_x} \xrightarrow{(\beta_2/2)2S_zI_x} \tag{69a}$$

and

$$\xrightarrow{(\beta_2/2)2S_zI_x} = \xrightarrow{-(\pi/2)I_y} \xrightarrow{(\beta_2/2)2S_zI_z} \xrightarrow{(\pi/2)I_y} \tag{69b}$$

The transfer of coherence for flip angles $\beta_2 = \pi$ and 2π is shown in Figure 38a. For $\beta_2 = \pi$, the density operator in eq 68 is represented by the pure zero quantum coherence $^1/_2(2S_xI_x + 2S_yI_y)$, which is not observable and also not affected by the refocusing mw π pulse. Thus, an rf pulse with flip angle $\beta_2 = \pi$ causes a full decay of the electron spin echo intensity (ENDOR efficiency $F_{ENDOR} = 0.5$). For $\beta_2 = 2\pi$, the single quantum coherence of transition $|\alpha\alpha\rangle \leftrightarrow |\beta\alpha\rangle$ changes sign, $-S_yI^\alpha$, and correspondingly, also the echo generated by a selective mw π pulse applied on this transition will change sign, resulting in an ENDOR efficiency $F_{ENDOR} = 1$. For $\beta_2 = 4\pi$ the phase factor returns to its original value. The sign change of the wave function after a 2π rotation and the corresponding 4π rotational symmetry is called *spinor behavior* and follows from basic quantum mechanics of spin $^1/_2$ particles.[81] Experimentally this spinor behavior has been demonstrated, for example, on a three-level system in NMR.[82]

In the following, three different coherence transfer ENDOR schemes are considered. If the rf field is only applied during the first time-interval τ (Figure 39a), the flip angle dependence of the echo intensity is found to be

$$I^{sel}_{echo} = \tfrac{1}{2} \cos(\beta_2/2) \tag{70}$$

For the calculation of I^{sel}_{echo}, also the effect of the two terms in eq 17, which commute with S_z has to be considered. They describe the free evolution of the coherence of the nuclear transition that is not affected by the selective rf pulse. Unfortunately, this scheme suffers from a pronounced Bloch–Siegert (BS) shift[83] of the ESR transition. This undesired effect shifts the resonance frequency of the electron spin by

$$\omega_{BS} = -\gamma_e(B_2^2/B_0) \tag{71}$$

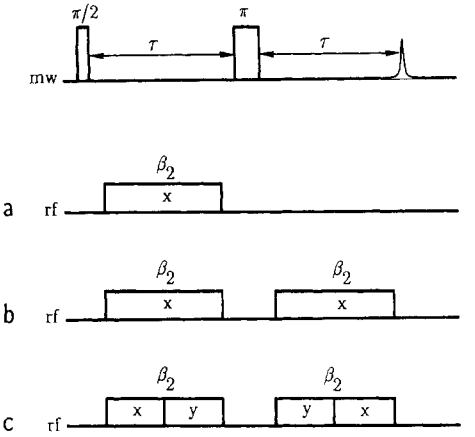

Figure 39. Pulse schemes for coherence transfer ENDOR. The labels x and y relate to the corresponding phase of the rf pulse: (a) rf pulse applied during the first τ-interval only, (b) rf pulse applied during both τ-intervals, and (c) as in b but with a phase change during the rf pulses.

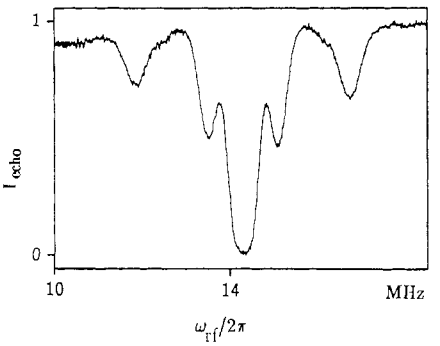

Figure 40. Coherence transfer ENDOR spectrum of the tri-*tert*-butyl phenoxyl radical in mineral oil at room temperature: concentration, 10^{-3} M; mw pulse lengths, $t^{\pi/2}_{mw} = 150$ ns, $t^{\pi}_{mw} = 300$ ns; $\tau = 950$ ns; rf power (tuned), 50 W (adapted from ref 42).

and causes for an rf pulse of duration τ a phase shift $\omega_{BS}\tau$ of the electron spin echo. Since the field strength B_2 is usually not constant during the sweep of the radiofrequency, the Bloch–Siegert shift shows up a broad feature across the ENDOR spectrum that can fully mask the ENDOR signal.

The effect of the Bloch–Siegert shift can be refocused by using an rf pulse sequence symmetric with respect to the mw π pulse (Figure 39b).[28] In this scheme, the dependence of the echo intensity on the rf flip angle is found to be

$$I^{sel}_{echo} = \tfrac{1}{2} \cos^2(\beta_2/2) \tag{72}$$

resulting in a maximum ENDOR efficiency for $\beta_2 = \pi$ of only $F_{ENDOR} = 0.5$.

An example of such a coherence transfer ENDOR experiment is shown in Figure 40.[42] It represents the first published pulsed ENDOR spectrum of a free radical in solution. The spectrum is recorded with an rf field of $B_2 = 2.7$ mT which is on during the whole mw pulse sequence. One of the drawbacks of such a coherence transfer ENDOR experiment becomes immediately evident from this spectrum. The width of the lines are strongly power broadened and, thus, considerably larger than in the corresponding cw ENDOR spectrum.[84] This is because of the short transverse electron spin relaxation time of $T_2 = 1.1$ μs that demands for a correspondingly short time interval τ be-

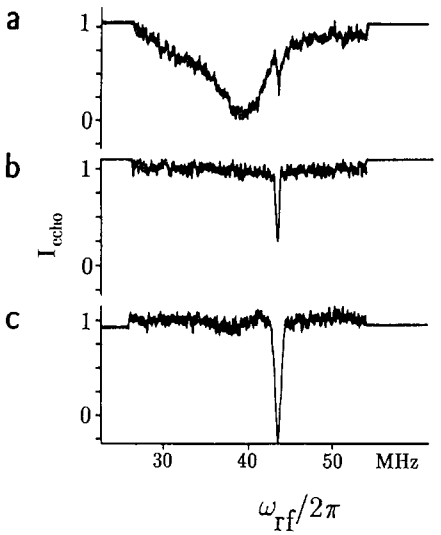

Figure 41. Coherence-transfer single-crystal ENDOR spectra of the malonic acid radical recorded with different pulse sequences, measured at room temperature: (a) rf pulse applied during the first τ interval (the broad feature observed in addition to the ENDOR line at 43 MHz is caused by the Bloch–Siegert shift), (b) two rf pulses applied symmetrically to the mw π pulse (the Bloch–Siegert shift is refocused), and (c) as in b but with a phase change during the rf pulses (the negative going line demonstrates that the ENDOR efficiency can be larger than 50%) (adapted from ref 28).

tween the two mw pulses. An other drawback is purely technical in origin. It is difficult to avoid getting a residual rf field component along B_0 which modulates the electron Zeeman frequency. This oscillations of the electron spin phase are particularly disturbing at low radio frequencies.[85]

The spinor effect that is eliminated by the symmetrization of the rf pulse sequence can, at least in principle, be recovered by the more sophisticated pulse scheme shown in Figure 39c.[28] For this sequence with 90° phase shifts during the rf pulses, the echo intensity is calculated to be

$$I^{sel}_{echo} = -\frac{1}{4}[1 + 2\cos(\beta_2/2) - \cos^2(\beta_2/2)] \quad (73)$$

For an rf flip angle of $\beta_2 = 2\pi$, the spinor behavior is fully reestablished ($F_{ENDOR} = 1$).

Figure 41 compares the ENDOR spectra of the malonic acid radical in the frequency range between 20 and 50 MHz obtained with the three coherence transfer ENDOR schemes of Figure 39. The broad feature in Figure 41a next to the sharp ENDOR line at 43 MHz is caused by the Bloch–Siegert shift. In the two sequences with rf pulses symmetric to the refocusing mw π pulse (Figure 41, parts b and c), this "contamination" is clearly avoided. With the phase-shifted spinor sequence the ENDOR efficiency is found to be larger than 0.5; however for technical reasons (rf field inhomogeneity), the theoretical limit is not fully achieved.[28]

It is straightforward to show that coherence transfer ENDOR experiments may also be carried out with nonselective mw pulses. Graphical representations for this case are shown in Figure 38b. A selective rf pulse with flip angle $\beta_2 = \pi$, for example, transfers the single quantum electron spin coherence S_y to both, pure zero and double quantum electron spin coherence, whereas for $\beta_2 = 2\pi$, the electron spin coherences of the two single quantum transitions change sign. This results in an echo intensity which (for a single spin packet) is twice as large as the one obtained with selective excitation.

The coherence transfer ENDOR methods described above are related to the nuclear–nuclear double resonance experiment introduced in NMR some time ago.[86] In this approach all the pulses are *nonselective* and consequently a free evolution period under a spin–spin coupling is required before coherence can be transferred. We have already mentioned above that in ENDOR the rf pulses are usually not able to cover the whole spectral range. The NMR scheme with nonselective pulses can therefore not be adapted to electron–nuclear double resonance.

VI. Concluding Remarks

In this review article the various pulsed ENDOR methods described in the literature so far are presented within the framework of a concise mathematical formalism, which allows one to directly follow the behavior of the spin system during the different time intervals of the experiment. Among these different approaches the polarization transfer ENDOR schemes are of primary interest. In order to polarize the nuclei in such an experiment, the first step always consists in the creation of electron–nuclear spin order ($2S_zI_z$, $4S_zI_{1z}I_{2z}$,...). This spin order can be prepared either by a single selective mw pulse or by a sequence of nonselective mw pulses together with a free evolution under a hyperfine interaction. In the following mixing period the nuclear polarization is manipulated in different ways by rf pulses. Finally, the effect of these manipulations is monitored with the help of the electron spin echo.

Basically different from this approach are the coherence transfer ENDOR experiments. Here, the first step consists in the creation of single quantum electron spin coherence. The rf pulse transfers this coherence to forbidden ESR transitions (zero and double quantum coherence). Consequently, the coherence is "stored" on a sidetrack that can no longer be affected by mw pulses (provided the transition probability for the forbidden transitions is zero), and has therefore no part in the echo formation.

After the discussion of all these new pulsed ENDOR techniques, the question raised is which of the sophisticated methodologies will have the potential for becoming established in the long term? The standard schemes introduced by Mims[9] and Davies[13] will undoubtedly become part of the everyday repertoire of pulsed ESR spectroscopy. Optimized polarization transfer ENDOR is useful for enhancing signal intensities; to be effective, however, the mw pulses have to be as short as possible. The 2D-ENDOR approach is easily implemented, requires no special instrumentation, and is very useful for the assignment of the transitions to particular nuclei. With hyperfine-selective ENDOR, single-crystal as well as powder ENDOR spectra may drastically be simplified. However, both the field-step and the frequency-step experiment require some additional instrumentation. As in cw triple resonance, pulsed triple is indicated for the determination of relative signs of hyperfine coupling constants and the separation of overlapped ENDOR spectra. Experimentally, introduction of a second rf field is straightforward. The indirect detection of nuclear

transient nutations and multiple quantum ENDOR proved to be very useful to study hyperfine spectral densities and to evaluate multiplicities. Incrementation of the rf pulse length in the former experiment is again straightforward, whereas the phase incrementation in the latter approach requires additional NMR instrumentation. Time-domain ENDOR is quite time-consuming and experimentally more elaborate. High rf fields are required and phase cycles have to be used. However, if ultimate resolution is demanded, this technique is certainly the method of choice. Coherence transfer ENDOR suffers from poor resolution caused by the short transverse electron spin relaxation time, the technique is therefore not of very general practical use.

Acknowledgments. We thank our colleagues for many helpful comments and suggestions. In particular we are grateful to Susanne Pfenninger and Thomas Wacker who have performed some of the measurements published in this work and to Richard R. Ernst for stimulating discussions regarding the theoretical description of pulsed ENDOR experiments. The manuscript has been processed by Mrs. Irene Müller. The Swiss National Science Foundation has financially supported this research.

VII. References

(1) Feher, G. *Phys. Rev.* **1956**, *103*, 834.
(2) Kevan, L.; Kispert, L. D. *Electron Spin Double Resonance Spectroscopy*; Wiley-Interscience: New York, 1976.
(3) Dorio, M., Freed, J. H., Eds. *Multiple Electron Resonance Spectroscopy*; Plenum: New York, 1979.
(4) Schweiger, A. *Struct. Bonding (Berlin)* **1982**, *51*, 1.
(5) Kurreck, H.; Kirste, B.; Lubitz, W. *Electron Nuclear Double Resonance Spectroscopy of Radicals in Solution*; VCH Publishers: New York, 1988.
(6) Möbius, K.; Plato, M.; Lubitz, W. *Phys. Rep.* **1982**, *87*, 171.
(7) Kurreck, H.; Kirste, B.; Lubitz, W. *Angew. Chem.* **1984**, *96*, 171; *Angew. Chem., Int. Ed. Engl.* **1984**, *23*, 173.
(8) Schweiger, A. *Electron Spin Reson.* (Specialist Periodical Reports, Symons, M. C. R., Ed.) **1987**, *10b*, 138.
(9) Mims, W. B. *Proc. R. Soc. London* **1965**, *283*, 452.
(10) Brown, I. M.; Sloop, D. J.; Ames, D. P. *Phys. Rev. Lett.* **1969**, *22*, 324.
(11) Brown, I. M.; Sloop, D. J. *Rev. Sci. Instrum.* **1970**, *41*, 1774.
(12) Liao, P. F.; Hartmann, S. R. *Phys. Rev.* **1973**, *B8*, 69.
(13) Davies, E. R. *Phys. Lett. A* **1974**, *47A*, 1.
(14) Stillman, A. E.; Schwartz, R. N. *Mol. Phys.* **1978**, *35*, 301.
(15) Merks, R. P. J.; de Beer, R.; van Ormondt, D. *Chem. Phys. Lett.* **1979**, *61*, 142.
(16) Poot, J.; Wenckebach, W. Th.; Poulis, N. J. *Physica* **1981**, *106b*, 368.
(17) de Beer, R.; Barkhuijsen, H.; de Wild, E. L.; Merks, R. P. J. *Bull. Magn. Reson.* **1981**, *2*, 420.
(18) Mims, W. B. In *Electron Paramagnetic Resonance*; Geschwind, S., Ed.; Plenum: New York, 1972; p 263.
(19) Salikhov, K. M.; Semenov, A. G.; Tsvetkov, Yu. D. *Electron Spin Echoes and their Applications*; Nauka: Novosibirsk, 1976.
(20) Kevan, L., Schwartz, R. N., Eds. *Time Domain Electron Spin Resonance*; Wiley: New York, 1979.
(21) Keijzers, C. P., Reijerse, E. J.; Schmidt, J., Eds. *Pulsed EPR*; North Holland: Amsterdam, 1989.
(22) Hoff, A. J., Ed. *Advanced EPR*; Elsevier: Amsterdam, 1989.
(23) Kevan, L., Bowman, M. K., Eds. *Modern Pulsed and Continuous Wave Electron Spin Resonance*; Wiley: New York, 1990.
(24) Schweiger, A. *Angew. Chem.* **1991**, *103*, 223; *Angew. Chem., Int. Ed. Engl.* **1991**, *30*, 265.
(25) van der Poel, W. A. J. A.; Singel, D. J.; Schmidt, J.; van der Waals, J. H. *Mol. Phys.* **1983**, *49*, 1017.
(26) Mehring, M.; Höfer, P.; Grupp, A.; Seidel, H. *Phys. Lett. A* **1984**, *106A*, 146.
(27) Höfer, P.; Grupp, A.; Mehring, M. *Phys. Rev. A* **1986**, *A33*, 3519.
(28) Mehring, M.; Höfer, P.; Grupp, A. *Phys. Rev. A* **1986**, *A33*, 3523.
(29) Grupp, A.; Höfer, P.; Käss, H.; Mehring, M.; Weizenhöfer, R.; Wegner, G. *Springer Ser. Solid-State Sci.* **1987**, *76*, 156.
(30) Käss, H.; Höfer, P.; Grupp, A.; Kahol, P. K.; Weizenhöfer, R.; Wegner, G.; Mehring, M. *Europhys. Lett.* **1987**, *4*, 947.
(31) Mehring, M.; Höfer, P.; Grupp, A. *J. Phys. Chem.* **1987**, *91*, 1132.
(32) Mehring, M.; Grupp, A.; Höfer, P.; Käss, H. *Synth. Met.* **1989**, *28*, D399.
(33) Mehring, M.; Höfer, P.; Käss, H.; Grupp, A. *Europhys. Lett.* **1988**, *6*, 463.
(34) Gemperle, C.; Schweiger, A.; Ernst, R. R. *Chem. Phys. Lett.* **1988**, *145*, 1.
(35) Gemperle, C.; Sørensen, O. W.; Schweiger, A.; Ernst, R. R. *J. Magn. Reson.* **1990**, *87*, 502.
(36) Bühlmann, C.; Schweiger, A.; Ernst, R. R. *Chem. Phys. Lett.* **1989**, *154*, 285.
(37) Thomann, H.; Bernardo, M. *Chem. Phys. Lett.* **1990**, *169*, 5.
(38) Thomann, H.; Bernardo, M.; Baldwin, M.; Lowery, M.; Solomon, E. I. *J. Am. Chem. Soc.* **1991**, *113*, 5911.
(39) Reijerse, E. J.; Klaassen, A. A. K. *Rev. Sci. Instrum.* **1986**, *57*, 2768.
(40) Reijerse, E. J.; van Aerle, N. A. J. M.; Keijzers, C. P.; Böttcher, R.; Kirmse, R.; Stach, J. *J. Magn. Reson.* **1986**, *67*, 114.
(41) Sloop, D. J.; Lin, T. S. *J. Magn. Reson.* **1990**, *86*, 156.
(42) Forrer, J.; Pfenninger, S.; Eisenegger, J.; Schweiger, A. *Rev. Sci. Instrum.* **1990**, *61*, 3360.
(43) Cho, H. *J. Chem. Phys.* **1991**, *94*, 2482.
(44) Höfer, P.; Grupp, A.; Mehring, M. In *Electronic Magnetic Resonance of the Solid State*; Weil, J. A., Bowman, M. K., Morton, J. R., Preston, K. F., Eds.; Can. Soc. Chem.: Ottawa, 1987; p 521.
(45) Mehring, M.; Höfer, P.; Grupp, A. *Ber. Bunsenges. Phys. Chem.* **1987**, *91*, 1132.
(46) Dinse, K. P. in ref 22, p 615.
(47) Grupp, A.; Mehring, M. in ref 23, p 195.
(48) Schweiger, A.; Graf, F.; Rist, G.; Günthard, Hs. H. *Chem. Phys.* **1976**, *17*, 155.
(49) Köhler, K.; Kirmse, R.; Böttcher, R.; Abram, U.; Gribnau, M. C. M.; Keijzers, C. P.; de Boer, E. *Chem. Phys.* **1990**, *143*, 83.
(50) Rudin, M.; Schweiger, A.; Günthard, Hs. H. *Mol. Phys.* **1982**, *46*, 1027.
(51) Böttcher, R.; Kirmse, R.; Stach, J.; Reijerse, E. J.; Keijzers, C. P. *Chem. Phys.* **1986**, *107*, 145.
(52) Rudin, M.; Schweiger, A.; Günthard, Hs. H. *J. Magn. Reson.* **1983**, *51*, 278.
(53) Schweiger, A.; Rudin, M.; Günthard, Hs. H. *Mol. Phys.* **1980**, *41*, 63.
(54) Schweiger, A.; Günthard, Hs. H. *Chem. Phys.* **1978**, *32*, 35.
(55) Rudin, M.; Schweiger, A.; Berchten, N.; Günthard, Hs. H. *Mol. Phys.* **1980**, *41*, 1317.
(56) Kita, S.; Hashimoto, M.; Iwaizumi, M. *J. Magn. Reson.* **1982**, *46*, 361.
(57) Kirmse, R.; Böttcher, R.; Keijzers, C. P. *Chem. Phys. Lett.* **1982**, *87*, 467.
(58) Sørensen, O. W.; Eich, G. W.; Levitt, M. H.; Bodenhausen, G.; Ernst, R. R. *Prog. NMR Spectrosc.* **1983**, *16*, 163.
(59) Ernst, R. R.; Bodenhausen, G.; Wokaun, A. *Principles of NMR in One and Two Dimensions*; Clarendon Press: Oxford, 1987.
(60) Weitekamp, D. P.; Garbow, J. R.; Pines, A. *J. Chem. Phys.* **1982**, *77*, 2870.
(61) Levitt, M. H. In *Two-Dimensional NMR and Related Techniques*; Brey, W. S., Ed.; Academic Press: New York, 1988; p 111.
(62) Sørensen, O. W. *Prog. NMR Spectrosc.* **1989**, *21*, 503.
(63) Abragam, A.; Bleaney, B. *Electron Paramagnetic Resonance of Transition Ions*; Clarendon Press: Oxford, 1970.
(64) Hagen, W. R. in ref 22, p 785.
(65) Wacker, T. Unpublished results.
(66) Gemperle, C. Unpublished results.
(67) Schweiger, A.; Günthard, Hs. H. *Mol. Phys.* **1981**, *42*, 283.
(68) Völkel, G.; Böttcher, R.; Brunner, W.; Milsch, B.; Pöppl, A.; Windsch, W. *Exp. Tech. Phys.* **1988**, *36*, 359.
(69) Schweiger, A. in ref 22, p 243.
(70) Dinse, K. P.; Biehl, R.; Möbius, K. *J. Chem. Phys.* **1974**, *61*, 4335.
(71) Cook, R. J.; Whiffen, D. H. *Proc. Phys. Soc.* **1964**, *84*, 845.
(72) Robinson, B. H.; Dalton, L. A.; Beth, A. H.; Dalton, L. R. *Chem. Phys.* **1976**, *18*, 321.
(73) Schweiger, A.; Rudin, M.; Günthard, Hs. H. *Chem. Phys. Lett.* **1983**, *95*, 285.
(74) Biehl, R.; Plato, M.; Möbius, K. *J. Chem. Phys.* **1975**, *63*, 3515.
(75) Höfer, P. Ph.D. Thesis, University of Stuttgart, 1988.
(76) Carrington, A.; McLachlan, A. D. *Introduction to Magnetic Resonance*; Harper & Row: New York, 1969.
(77) Freeman, R.; Frenkiel, T. A.; Levitt, M. H. *J. Mag. Reson.* **1981**, *44*, 409.
(78) Gorlov, A. D.; Potapov, A. P.; Sherstkov, Yu. A. *Sov. Phys. Solid State* **1985**, *27*, 1726.
(79) Atherton, N. M.; Shackleton, J. F. *Mol. Phys.* **1980**, *39*, 1471.

(80) Atherton, N. M.; Horsewill, A. J. *Mol. Phys.* **1979**, *37*, 1349.
(81) Messiah, A. *Quantum Mechanics*; North-Holland: Amsterdam, 1961.
(82) Stoll, M. E.; Wolff, E. K.; Mehring, M. *Phys. Rev.* **1978**, *A17*, 1561.
(83) Bloch, F.; Siegert, A. *Phys. Rev.* **1940**, *57*, 522.
(84) Allendoerfer, R.; Maki, A. H. *J. Magn. Reson.* **1970**, *3*, 396.
(85) Mims, W. B. Private communication.
(86) Emshwiller, M.; Hahn, E. L.; Kaplan, D. *Phys. Rev.* **1960**, *118*, 414.